Tribology International 200 (2024) 110172

Contents lists available at ScienceDirect

Tribology International

journal homepage: www.elsevier.com/locate/triboint

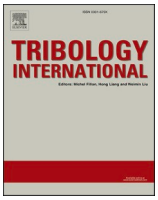

Remarkable enhancement of the corrosive-wear resistance for Ti-Zr-Hf-Nb-Fe high-entropy alloys by a facile high-temperature oxidation treatment

Nengbin Hua [a,c,*], Yang Xu [a,c], Bozhuan Lin [a,c], Da Zeng [b], Xiongwei Liang [b], Xinxiong Xiao [b], Hanxin Lin [a,c], Lei Zhang [a,c], Wenfei Lu [a,c], Pinqiang Dai [a,c], Qianting Wang [a,c], Jun Shen [a,c], Peter K. Liaw [d]

[a] School of Materials Science and Engineering, Fujian University of Technology, Fuzhou 350118, China
[b] Double Medical Technology Co., Ltd, Xiamen 361026, China
[c] Fujian Provincial Key Laboratory of Advanced Materials Processing and Application, Fujian University of Technology, Fuzhou 350118, China
[d] Department of Materials Science and Engineering, The University of Tennessee, 37996-2200 Knoxville, TN, USA

ARTICLE INFO

Keywords:
Refractory high-entropy alloys
Oxidation behavior
Oxidation mechanism
Wear resistance

ABSTRACT

The surface performances of TiZrHfNbFe refractory high-entropy alloys (RHEAs) were improved by a facile oxidation treatment at 1000 °C. Results indicated that the anomalous retarded oxidation behavior of the RHEA enabled the formation of a dense and robust oxide layer, demonstrating superior wear and corrosion resistance. The oxidation resistance of the RHEA was related to the development of Ti_2ZrO_6 on the surface and acicular HfO_2 in the inner oxide layer. Additionally, the oxidation mechanism of the RHEA was elucidated, based on principles of oxidation thermodynamics and kinetics, providing foundations for applications as implant materials.

1. Introduction

Owing to their favorable mechanical properties, excellent resistance to corrosion, and biocompatibility, Ti-based alloys have been extensively utilized in clinical fields as biomaterials [1–7], including applications in artificial hip joints, knee joints, bone plates, vascular scaffolds, and dental implants, etc. [8–11]. Despite their numerous advantages in clinical practice, Ti-based alloys still face a number of unresolved challenges as artificial joint materials. These factors include the "stress shielding effect" resulting from the disparity of Young's moduli between implants and bones in humans [12–15], the biotoxic allergic reactions triggered by the emission of noxious ions [16–18], and the "particle disease" caused by the insufficient resistance to wear of Ti-based alloys [19–21].

Given the enduring mechanical stresses to which artificial joints are subjected, it is imperative for the materials to exhibit superior wear resistance, thereby ensuring the long-term stability and durability of the joint prostheses [19–21]. In pursuit of the enhanced wear resistance in Ti-based alloys, extensive research efforts have been directed towards surface-modification strategies for these materials, encompassing thermal oxidation, nitridation, physical vapor deposition, chemical vapor deposition, and laser cladding, etc. [22–27]. Of these methodologies, surface-thermal oxidation has emerged as a particularly appealing option due to its simplicity, cost-effectiveness, and precise control over coating thickness positioning it as a highly promising technique with significant potential for practical applications.

Investigations into the thermal oxidation of various Ti-based alloys have been conducted [28–32]. For instance, Kumar et al. reported a nearly sixfold increase in the hardness of CP Ti samples after oxidation at 800 °C, accompanied by a decrease in the passivation current density by approximately 500-fold [33]. Wang et al. examined the wear behavior of β-Ti samples subjected to an oxygen-filled heat treatment at 1000 °C and observed a threefold reduction in the wear rate of the thermally oxidized β-Ti samples, compared to their unoxidized counterparts, indicating a marked enhancement in wear resistance [34]. Additionally, the effect of oxidation treatment on the Ti6Al4V alloy at 600 °C was investigated, which showed a significant increase in the hardness and a 25-fold improvement in the wear resistance of the treated samples relative to as-cast specimens [35].

The control of oxidation processes of alloy surfaces takes a critical

* Corresponding author at: School of Materials Science and Engineering, Fujian University of Technology, Fuzhou 350118, China.
E-mail address: flower1982cn@126.com (N. Hua).

https://doi.org/10.1016/j.triboint.2024.110172
Received 21 July 2024; Received in revised form 13 August 2024; Accepted 26 August 2024
Available online 28 August 2024

influence in determining the properties of Ti-based alloys. For instance, Latief et al. observed a decrease in the hardness on the surface of the pure Ti and the appearance of cracks in the surface oxide film after being oxidized at 900 °C [28]. Meanwhile, Zhong et al. reported that the notable disparity in thermal-expansion coefficients between the matrix and oxide in the near-α Ti-based alloys caused the development of cracks in the oxide layer [29]. In addition, Wang et al. discovered that during the oxidation process of the Ti6Al4V alloy, the adhesion between the matrix and oxide film was diminished, while cracks appeared in the oxide layer [36]. Furthermore, the studies on the properties of the Ti-based alloys at elevated oxidation temperatures showed that [30,31] the wear rates of Ti6Al4V and Ti6Al7Nb alloys were increased at 700 °C, and the tensile performances of Ti6Al7Nb samples were deteriorated at 800 °C [37]. Similarly, López et al. reported multiple pores and cracks at the interface between the metal and oxide after the prolonged oxidation treatment of the TiZrNb alloy at 750 °C, which resulted in the spallation of the oxide layer and a decrease in anticorrosion performance [32]. Overall, these findings suggest that an inappropriate thermal-oxidation treatment process can result in the formation of unstable oxide films on Ti-based alloy surfaces, characterized by delamination, porosity, and cracking, ultimately turning into a decrease in their mechanical, anti-wear, and anticorrosion properties.

In recent years, high-entropy alloys (HEAs), consisting of elements in ratios ranging from 5 to 35 at. percent (at%), have garnered significant attention due to their exceptional comprehensive properties, including high strength, great ductility, superior elevated-temperature performance, and excellent wear and corrosion resistance [38–54]. Among these alloys, refractory high-entropy alloys (RHEAs) primarily comprised of refractory elements, such as Ti, Zr, Nb, Hf, Ta, W, and others, have been successfully developed [55]. The high-entropy and hysteretic diffusion effects of HEAs may mitigate or resolve oxide-film delamination. Presently, the thermal-oxidation behaviors of various RHEAs have been extensively investigated. Li et al. discovered that TiZrHfNb RHEAs with varying Al contents exhibited equiaxed grain structures and a continuous and dense surface-oxide layer by heat treatment, significantly improving their yield strengths together with the wear resistance of the alloy [56]. Jin et al. observed that a compact glazing surficial-oxide layer developed on the $TiZrNbMo_{0.6}$ RHEA at 500 °C, which could protect the matrix and decrease the wear rate [57]. Xu et al. found that the antiwear and anticorrosion performance of the TiZrNbTaMo RHEA were notably enhanced, following the thermal-oxidation treatment in air [58].

In our previous study, we found that the $TiZrHfNbFe_{0.5}$ RHEA exhibited superior mechanical properties (with a higher strength compared to the Ti6Al4V and an elastic modulus of approximately 50 GPa, a value comparable to that of human bone) and wear resistance [59]. The objective of the present investigation is to develop an artificial joint material intended for use in biomedical implants. In this paper, we discovered that the $TiZrHfNbFe_{0.5}$ RHEA exhibited “abnormal” oxidation behavior under the heating condition at 1000 °C for 6 h. As a result, a dense and stable surface protective layer through oxidation, demonstrating excellent wear resistance, high corrosion resistance, and good biocompatibility. Subsequently, we investigated its oxidation mechanisms. A salient feature of this research is the substantial enhancement in wear resistance accomplished by the formation of a ceramic oxide layer on the surface of high-entropy alloys via surface oxidation heat treatment. This treatment ensures that the underlying metal matrix preserves the inherent advantages of metallic materials, providing both theoretical and experimental foundations for its potential application as artificial joint material.

2. Experimental

2.1. Sample preparation

The Ti, Hf, Nb, Zr, Ta, and Fe raw materials with a high-purity above 99.9 wt percent (wt%) were mixed in accordance with the nominal composition of the TiZrHfNbTa (equal molar ratios) and $TiZrHfNbFe_x$ (x = 0, 0.5, 1, 1.5, and 2, molar ratio), where $TiZrHfNbFe_{0.5}$ was denoted as $TZHNF_{0.5}$ for the abbreviation. To achieve chemical homogeneity, the samples underwent arc-melting at least five times in a water-cooled copper crucible under an argon environment. The Ti6Al4V alloy was employed as a reference material. Using wire electrical discharge machining (WEDM), specimens with dimensions of ($10 \times 10 \times 2$ mm^3) and ($3 \times 3 \times 2$ mm^3) were sliced from the innermost part of the alloy ingot. The samples are ground with SiC sandpaper and then polished with a polishing machine (UNIPOL-830). Finally, the alloy samples were ultrasonically cleaned, using ethanol and deionized water, followed by air drying for subsequent performance testing.

2.2. Structural characterization

The crystal structures of the RHEAs were investigated, using a Bruker-AXS-D8 X-ray diffractometer (XRD). X-ray diffraction analysis was conducted at 40 kV and 40 mA, employing a scan rate of 6°/min., a scan range of 2θ from 20° to 80°, and a step size of 0.02°. The surface morphology of the RHEAs was characterized, using both the Nova Nano SEM 450 field emission scanning electron microscope and the S-3400 N scanning electron microscope (SEM), while component evaluation was performed, utilizing an accompanying energy-dispersion spectrometer (EDS). The phase and composition analysis of the as-cast $TZHNF_{0.5}$ RHEA and the oxide region layer following oxidation at 1000 °C for 6 h were conducted utilizing the FEI Helios NanoLab 600i focused ion beam (FIB) and Talos F200X transmission electron microscope (TEM) attached with the EDS.

2.3. Oxidation experiments

The as-cast alloy samples were subjected to thermal-oxidation experiments in a high-temperature furnace. The oxidation tests of the alloys were performed at 300 °C, 400 °C, 600 °C, 800 °C, 1000 °C, 1100 °C, and 1200 °C for 6 h, with a heating rate of 10 °C/min. Prior to the experiment, weights of individual alloy blocks and the combined weight of the blocks and crucible were measured, by an electronic balance with (deploying a precise electronic scale with) a precision of 0.1 mg. The sample was immediately placed in the heating furnace when the set temperature was reached, and it was removed and cooled after every hour, measuring the weight of the individual block and the total weight. It was then immediately returned to the furnace for further oxidation, consistent with the methods described in relevant literature [60]. To evaluate the modification in the microstructure within the $TZHNF_{0.5}$ RHEA oxide layer after 6 h of oxidation at 1000 °C, grinding and polishing were performed in different depth regions. The microstructures and morphologies of the different depth regions were characterized using XRD, SEM, and EDS, for the observation of the microstructural evolution with depth within the oxide layer and transition layer.

2.4. Mechanical properties

The as-cast and oxidized $TZHNF_{0.5}$ RHEA specimens were subjected to micro-Vickers hardness testing using a THVP-10 micro-Vickers hardness tester. The test load was set at 3 kgf, and the holding time was 15 s. To ensure reproducibility, at least five measurements were made on each specimen.

2.5. Wear behaviors

In this study, we employed the HSR-2 T reciprocating-sliding friction and wear-testing machine, using a 6-mm-diameter Si_3N_4 ball as the counter face, to investigate the tribological parameters of the alloys. The friction and wear tests were divided into dry and wet-friction experiments. The dry-friction test was conducted in a room-temperature air

environment, while the wet-friction experiment was conducted in a phosphate-buffered saline (PBS) solution at room temperature. The experimental environments were chosen as follows: a normal load of 20 N, a sliding duration of 30 min, a rotational speed of 200 rpm, and a friction stroke of 5 mm. The coefficient of friction (COF) was evaluated throughout the sliding process. A MT-500 probe-type material-surface profilometer was introduced to identify the wear-scar volume. Additionally, we observed the wear-scar morphology on the worn surface using SEM and analyzed the surface composition by EDS.

2.6. Corrosion behaviors

The electrochemical characteristics of the RHEA samples in a PBS solution were tested using an AutoLab electrochemical workstation. A three-electrode system, consisting of a platinum sheet counter electrode, a saturated calomel reference electrode (SCE), and a sample working electrode, was employed to test the dynamic-potentiodynamic-polarization curves of the samples. The corrosion morphology of the polarized samples was examined through SEM.

To further investigate the corrosion mechanism of the alloy in the PBS solution, the surface-chemical characteristics of the passivation film on the cast alloy surface and on the alloy surface after being submerged in the PBS for a period of 24 h were measured through an ESCALab250 X-ray photoelectron spectrometer (XPS). The narrow scan spectra of elements, such as Ti 2p, Hf 4 f, Fe 3d, Zr 3d, Nb 3d, and O 1 s, in the alloy were measured.

2.7. Surface-bioactivity experiment

The bioactivity of the as-cast and 1000 °C-oxidized $TZHNF_{0.5}$ RHEA specimens was evaluated through immersion experiments. The samples were maintained at 37 °C in a simulated body fluid (SBF) solution for 14 days. Following the experiment, the immersed samples underwent cleaning and drying, using deionized water. The morphology of the alloy surface after immersion was examined through SEM, and the elemental composition was determined using EDS. The formation of hydroxyapatite on the alloy surface with an emphasis on the distribution of Ca and P elements. The SBF-solution composition was described as follows: NaCl 8.035 g, KCl 0.225 g, $CaCl_2$ 0.292 g, $NaHCO_3$ 0.355 g, Na_2SO_4 0.072 g, $K_2HPO_4{\cdot}3\ H_2O$ 0.231 g, $MgCl_2{\cdot}6\ H_2O$ 0.311 g, $NH_2C(CH_2OH)_3$ 6.118 g, and HCl (1 M) 39 ml.

3. Results

3.1. Macroscopic-surface morphology of RHEAs after oxidation

Fig. 1 displays the macroscopic-surface characteristics of RHEAs with different compositions as well as the Ti6Al4V alloy after oxidation at temperatures ranging from 400 °C to 1100 °C for 6 h. The Ti6Al4V alloy, when oxidized at 400 °C and 600 °C, presents a light yellow and light purple color on the surface. When the oxidation temperature reaches 800 °C, the surface layer of the Ti6Al4V becomes darker, and the delamination of the oxide layer occurs. At temperatures beyond 1000 °C, the surface oxide layer of the Ti6Al4V becomes looser, and the delamination phenomenon is more serious. The surface-oxide layers of the TiZrHfNb and TiZrHfNbTa RHEAs being oxidized at 400 °C and 600 °C are dark gray, accompanied by the delamination of the oxide layer. When the oxidation temperature reaches 800 °C, both alloys undergo intense oxidation, and the entire alloy sample turns into white powders after oxidation for 6 h. At temperatures above 1000 °C, the oxidation resistance of the TiZrHfNb and TiZrHfNbTa RHEAs is relatively improved, but the surface oxide layer is white, and the delamination of the surface layer is still serious.

At 400 °C, the surface-oxide layer of the TiZrHfNbFe RHEAs exhibits a dark gray hue. When heating at 600 °C and 800 °C, the surface-oxide layer transitions to a reddish-brown coloration, accompanied by the delamination of the oxide layer. Interestingly, upon reaching 1000 °C, the surface-oxide layer of the TiZrHfNbFe RHEAs transforms to a dark gray hue, manifesting superior surface integrity. In particular, the $TZHNF_{0.5}$ RHEA demonstrates no delamination of the oxide layer, and

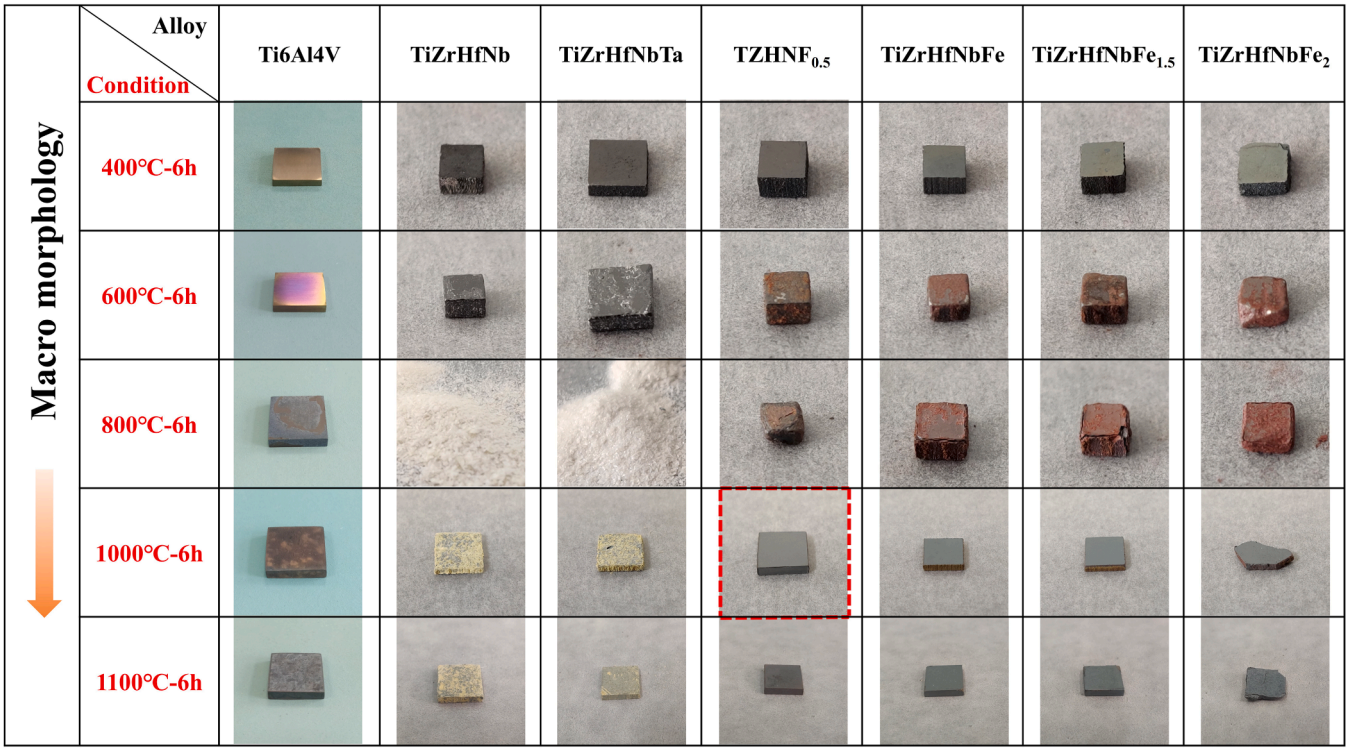

Fig. 1. The macroscopic-surface characteristics of RHEAs with different compositions as well as the Ti6Al4V alloy after oxidation at temperatures ranging from 400 °C to 1100 °C for 6 h.

the oxide-layer surface remains smooth and flat. Upon further elevation of the temperature to 1100 °C, the surface-oxide layer of the TiZrHfNbFe RHEAs displays a certain degree of delamination. Overall, 800 °C represents the intense oxidation stage for all alloys, and their oxidation resistance is at the lowest for this temperature. The oxide layer formed by the $TZHNF_{0.5}$ RHEA at 1000 °C possesses remarkable stability.

3.2. Oxidation kinetics of RHEAs

Fig. 2(a) depicts the unit-area weight gain of the $TZHNF_{0.5}$ RHEA oxidized at various temperatures and durations, with fitted curves of the oxidation weight-gain data points. Overall, the weight gain of the $TZHNF_{0.5}$ RHEA increases with elevating the oxidation temperature and prolonging the oxidation duration, especially at 1200 °C, where the oxidation weight gain exhibits an approximately linear increase trend with the extended oxidation time. Interestingly, the weight-gain kinetics curve of the RHEA at 1000 °C significantly differs in shape from those at other temperatures. At an elevation of 1000 °C, the RHEA has a sharp rise in the oxidation-weight elevation during the initial 15 min, which is afterwards followed by a progressive decline in the rate of the oxidation-weight gain, and when the oxidation duration exceeds 3 h, the oxidation-weight gain remains virtually unchanged, which is notably smaller than that at 800 °C. This trend indicates that the $TZHNF_{0.5}$ RHEA demonstrates a stable oxidation-kinetics phenomenon at the heating temperature of 1000 °C.

In Fig. 1, we can observe the phenomenon of oxide-scale spalling in the $TZHNF_{0.5}$ RHEA under certain temperature conditions. Fig. 2(b) presents the plot of the oxidation-weight loss per unit area of the $TZHNF_{0.5}$ RHEA vs. the oxidation duration at various temperatures. The oxidation-weight loss is defined as the change in the weight of the alloy specimen after removing the oxidized spalling powder. Initially, at 1200 °C, the $TZHNF_{0.5}$ RHEA exhibits a significant increase in the oxidation weight, but when the oxidation time exceeds 2 h, a noticeable weight loss is observed, indicating that the intense oxidation and oxide-layer spalling at this temperature. Similarly, slight weight losses are also observed in the later stages of oxidation at 600 °C and 800 °C. In contrast, no significant weight loss is observed during the oxidation process at 400 °C and 1000 °C, suggesting that the surface oxide layer remains relatively intact and stable at these temperatures.

The weight-gain curve of the alloy during oxidation is fitted using the commonly employed oxidation law Eq. (1) [61]:

$$\frac{\Delta m}{S} = kt^n \tag{1}$$

where Δm represents the oxidation-weight gain, S denotes the entire area of the surface of the alloy, k acts as the constant that controls the oxidation-growth rate (a smaller k value indicates a slower oxide-scale growth), t represents the oxidation period, and n is the time exponent. When $n = 0.5$, the alloy-oxidation is said to be in accordance with a parabolic law, while $n = 1$ points to a linear law.

The oxidation-time exponent of the $TZHNF_{0.5}$ RHEA approaches 0.5 when heated at 400 °C, 600 °C, and 800 °C, which results in a parabolic-like oxidation-growth curve. This trend exhibits the capability of the RHEA to generate a defensive-surface layer, thereby isolating the oxygen from directly interacting with the metal substrate. Thus, oxygen should diffuse inward through the oxide layer and react with the metallic substrate. However, as heated at 1200 °C, the oxidation-time exponent of the RHEA approaches 1, which refers to a linear-like oxidation-growth curve. This feature indicates that the surface-oxide layer is relatively porous and renders inadequate protection to the alloy substrate, which results in the direct interaction between oxygen with the metallic substrate [62].

As heated at 1000 °C, the oxidation-time exponent of the RHEA is 0.123, which implies that the oxidation mechanism of the alloy experiences a sudden change and then remains consistent during the balance of the oxidation period [63]. This trend corresponds to the stable response illustrated and exhibited in Fig. 1. Prior studies have found that the Ti6Al4V alloy displays reduced resistance to oxidation at 1000 °C during oxidation experiments, with an oxidation time exponent approaching 1 and an oxidation-growth curve that closely follows a linear fit [64]. The surface of the oxide layer becomes porous and rough, making it susceptible to flaking, which highlights its lower antioxidant properties.

3.3. Oxidation products and microstructures of RHEAs

Fig. 3(a-c) present the XRD patterns of the as-cast $TZHNF_{0.5}$ RHEA and the corresponding alloy oxidized under different temperatures. The oxidized bulk sample denotes the bulk sample, while the powder sample represents the oxidation-spalling product. In Fig. 3(a), it can be observed that the as-cast $TZHNF_{0.5}$ RHEA is comprised of body-centered-cubic (BCC) and Laves phases. With enhancing the heating temperature, the fractions of the BCC and Laves phases decrease, accompanied by the formation of new phases, which is likely linked to the formation of oxides. Upon reaching an oxidation temperature of 400 °C, a modest amount of Fe_2O_3 oxide begins to emerge on the alloy surface. Fig. 3(b) shows that when the oxidation temperature rises to 600 °C and 800 °C, a substantial amount of Fe_2O_3 and Nb_2O_5 oxides are identified.

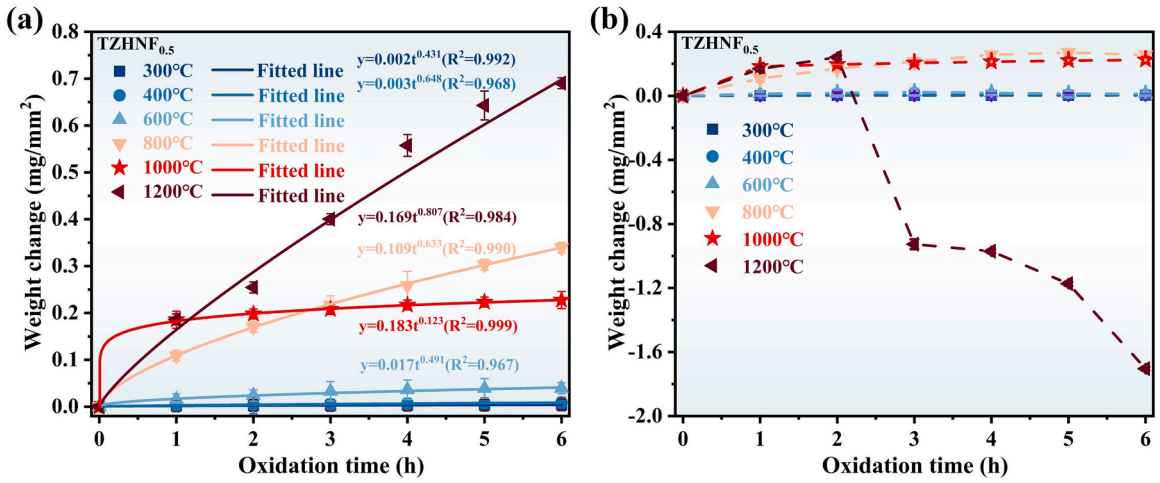

Fig. 2. Oxidation-kinetics curves of the $TZHNF_{0.5}$ RHEA vs. the oxidation duration at various temperatures: (a) oxidation-unit area weight gain and fitting curve, and (b) oxidation-weight loss per unit area.

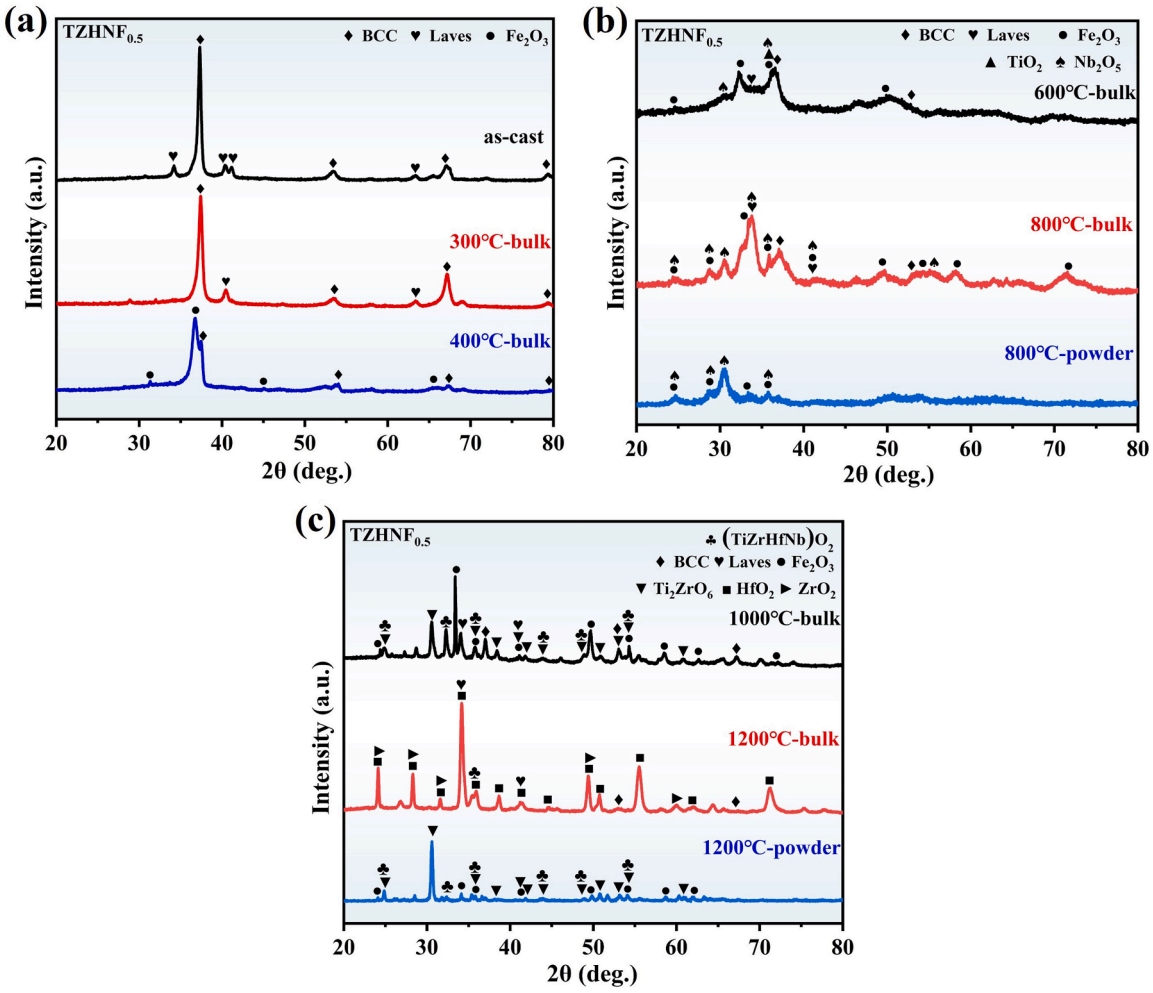

Fig. 3. (a-c) XRD patterns of the as-cast $TZHNF_{0.5}$ RHEA and the corresponding alloy oxidized under different temperatures.

The strong expansivity of Nb_2O_5 can lead to cracks in the oxide layer, which creates pathways for the rapid oxygen penetration, resulting in the spalling and delamination of the surface-oxide layer [65]. The XRD analysis of the oxidized products spalled from the alloy surface after oxidation shows that they are primarily Nb_2O_5 and Fe_2O_3. In Fig. 3(c), after oxidizing the alloy at 1000 °C, the primary oxides formed are Ti_2ZrO_6 and Fe_2O_3, and a new composite oxide of $(TiZrHfNb)O_2$ appears on the surface [66]. Among them, the Ti_2ZrO_6 oxide facilitates the formation of a more complete oxide layer, thus slowing the oxidation rate [67]. After the oxidation temperature reaches 1200 °C, the alloy surface experiences severe spalling, and the exposed surface after spalling is composed of oxides, such as HfO_2 and ZrO_2. The spalled oxides are primarily Ti_2ZrO_6, Fe_2O_3, and the composite oxide $(TiZrHfNb)O_2$.

Fig. 4(a-g) show the SEM-surface morphology of the as-cast $TZHNF_{0.5}$ RHEA, and the corresponding alloy oxidized at different temperatures. Fig. S1 presents the EDS-analysis results corresponding to the characteristic regions in Fig. 4. As exhibited in Fig. 4(a), the as-cast alloy forms a typical dual-phase dendritic microstructure with a bright contrast dendritic phase and a dark contrast interdendritic phase. The EDS-analysis results reveal that both the dendritic phase and the interdendritic region incorporate Ti, Zr, Hf, Nb, and Fe elements. The composition of the light contrast dendritic phase shows a depletion of Fe and an enrichment of Nb, while the composition of the dark-contrast interdendritic region is converse, as a result of the preferential precipitation of the high-melting point Nb element during solidification, which accumulates in the dendritic region, and low-melting point Fe element, which aggregates in the interdendritic region due to the compositional segregation. In conjunction with the XRD analysis, it can be concluded that the dendritic region is primarily a BCC phase, and the interdendritic region is primarily a Laves phase, which is identified as an $Fe_2(TiZrHf)$ intermetallic compound.

Figs. 4(b) and 4(c) illustrate the surface-SEM morphology of the oxidized alloy heating at 300 °C and 400 °C. Despite the elevated temperature, the surface maintains a bimodal dendritic microstructure with relatively brief and coarse dendritic arms. As presented in Fig. S1, the surface composition consists of Ti, Nb, Hf, Zr, Fe, and O elements. The dendritic region is characterized by a depletion of Fe and an enrichment of Nb, while the interdendritic region is marked by a surplus of Fe. It is noteworthy that the fraction of the O element on the oxidized alloy surface heating at 400 °C is larger than that after oxidation at 300 °C, which corresponds to the oxidation-kinetic analysis.

Following oxidation at 600 °C, 800 °C, and 1000 °C, the alloy surface undergoes a transition from short and coarse dendritic structures to long and slender dendritic structures, as depicted in Fig. 4(d-f). With increasing temperature, the dendritic arms become increasingly finer and longer, and the volume fraction of interdendritic structures increases. Noteworthily, the surface morphology of the oxidized RHEA heating at 800 °C is comparable to that oxidized at 300 °C and 400 °C, which is primarily attributed to the peeling-off of the outermost oxide layer, exposing the region adjacent to the alloy substrate. This finding suggests that oxidation can give rise to modifications in the microstructural morphology of the alloy surface, culminating in the formation of long and slender dendritic structures. With elevating the oxidation temperature, the fractions of the Fe and O in the interdendritic region

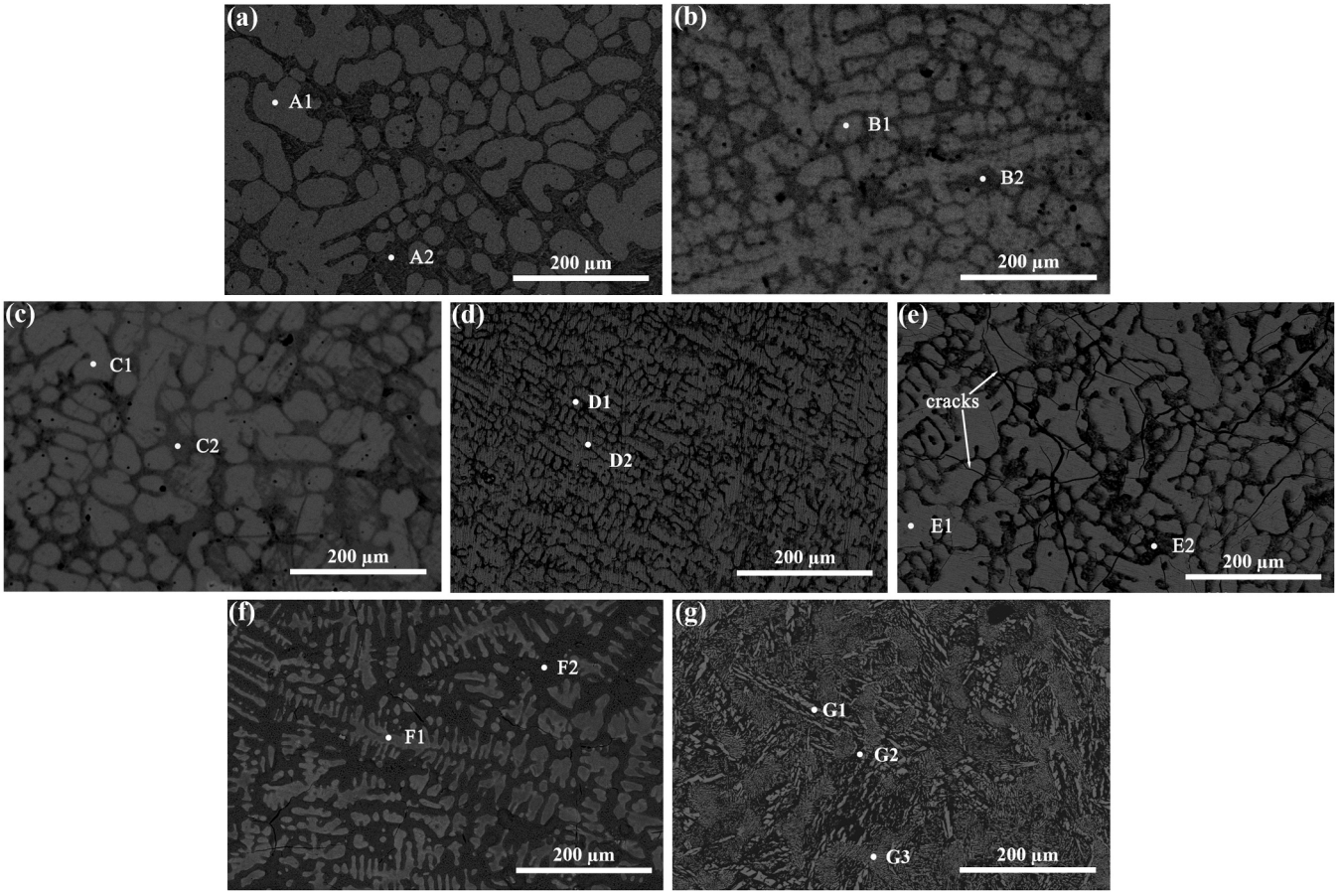

Fig. 4. SEM-surface morphology of the as-cast $TZHNF_{0.5}$ RHEA and the corresponding alloy oxidized at different temperatures. (a) as-cast state and oxidized states at (b) 300 °C, (c) 400 °C, (d) 600 °C, (e) 800 °C, (f) 1000 °C, and (g) 1200 °C.

progressively rise, while the contents of the other elements progressively decrease. Consequently, the degree of oxidation intensifies being heated at 600 °C and 800 °C, as evidenced by the severe exfoliation and delamination of the oxide layer observed in the macroscopic morphology depicted in Fig. 1, signifying inferior antioxidant performance.

At the elevated temperature of 1000 °C during oxidation, the alloy surface demonstrates a relatively elevated concentration of the Ti element. In conjunction with the XRD and EDS analyses, it is ascertained that the Ti_2ZrO_6 oxide forms within the dendritic region on the alloy surface, contributing to the stabilization of the surface-oxide layer for the RHEA. As a result, a relatively smooth oxidation weight-gain curve is observed, as exemplified in Fig. 2.

Fig. 4(g) illustrates that the surface-oxide layer of the RHEA undergoes spalling being heated at 1200 °C. In contrast to the situation heating at 1000 °C, the bulk-alloy surface displays substantial alterations, consisting of elongated needle-like structures (G1 region), as well as the original dendritic structures (G3 region) and interdendritic structures (G2 region). The results of the EDS analysis reveal that the G1 needle-like structure region is enriched in Zr and Hf elements, suggesting the formation of oxides, such as HfO_2 and ZrO_2, whereas the composition of the interdendritic region indicates a tendency towards the enrichment in Ti and Nb elements. Furthermore, the fraction of Fe is relatively reduced on the alloy surface. Moreover, the occurrence of the oxidation layer spalling on the alloy surface, characterized by dense laminations, cracks, and voids, further accelerates the oxidation process of the alloy, manifesting vigorous oxidative behavior. Previously reported investigations have proposed that these minute irregular pores, and numerous voids might be attributable to volumetric changes resulting from the formation of the fine needle-like HfO_2 and rapid segregation of Hf [68].

Fig. 5(a-f) present the cross-sectional SEM images of the $TZHNF_{0.5}$ RHEA after oxidation for 6 h at various temperatures. It can be noted that the surface-oxide layer exhibits a thickness of approximately 0.09 μm at 300 °C and 1 μm at 400 °C, respectively. As heated at 600 °C and 800 °C, the surface-oxide layer's thickness is approximately 26 μm and 168 μm, respectively. After oxidation at 800 °C, the surface layer exhibits visible fractures and holes, indicating the occurrence of spalling of the oxide layer. At 1000 °C oxidation, the thickness of the surface layer reaches 182 μm, and no obvious pores and cracks are present on the alloy surface, suggesting good densification.

The results presented in Fig. 5(g) provide insights into the cross-sectional microstructure of the $TZHNF_{0.5}$ RHEA and the elemental distribution within the oxide layer. The analysis reveals the presence of Nb-rich dendritic phases and Fe, Ti-rich interdendritic phases in the alloy, which aligns with earlier research on comparable alloys. Additionally, the oxygen content within the oxide layer is found to decrease gradually from the outer towards the inner regions, which suggests a gradient in the oxidation behavior of the alloy. Fig. 5(f) demonstrates the effect of elevated-temperature oxidation on the alloy-surface layer. After exposure to 1200 °C for 6 h, the surface layer is observed to have undergone spalling, with a residual portion remaining on the alloy surface. The residual-oxide layer shows a thickness of approximately 47 μm. From the cross-sectional perspective, the oxide layer consists of fine needle-like and small-particle regions. Moreover, numerous holes are observed in the surface layer, which results from the volumetric expansion of oxides during the heat treatment.

The oxide spalling in Fig. 5(f) merely occurred within the fine needle-

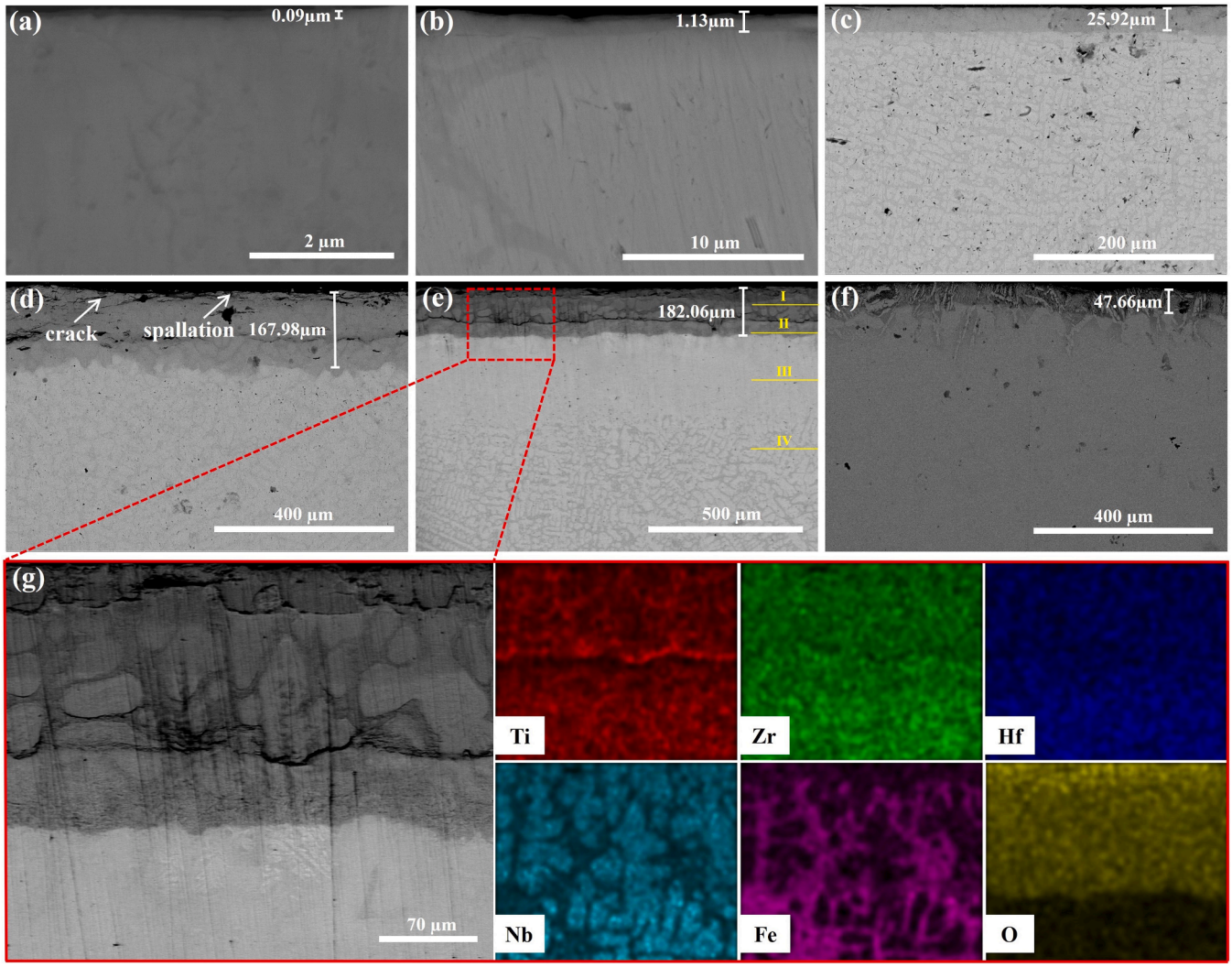

Fig. 5. Cross-sectional SEM images of the TZHNF0.5 RHEA after oxidation for 6 h at various temperatures: (a) 300 °C, (b) 400 °C, (c) 600 °C, (d) 800 °C, (e) 1000 °C, and (f) 1200 °C. (g) insights into the cross-sectional microstructure of the $TZHNF_{0.5}$ RHEA and the elemental distribution within the oxide layer.

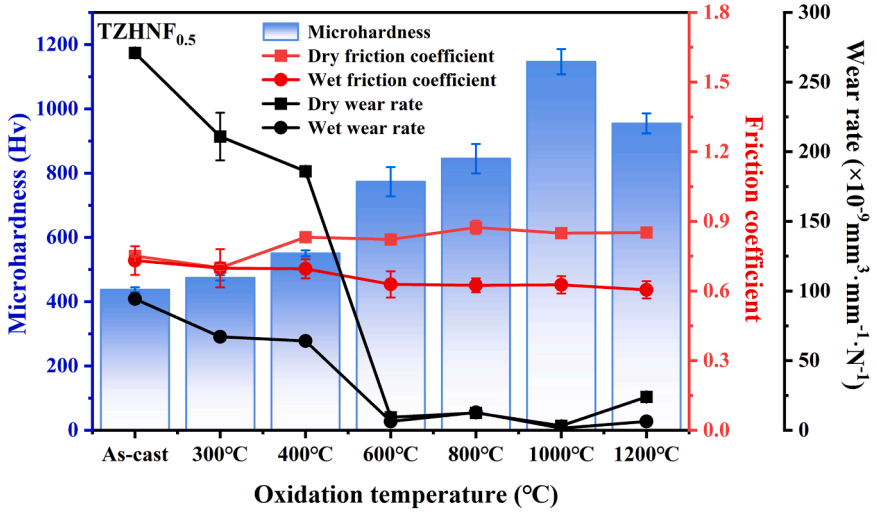

Fig. 6. Surface hardness, average friction coefficients, and wear rates of the $TZHNF_{0.5}$ RHEA in both the as-cast and oxidized states with various heating temperatures.

like region. It can be inferred that the formation of numerous fine needle-like HfO_2 phases reduces the bonding strength between the oxide film and the metallic matrix. Nevertheless, the surface layer undergoes oxide spalling, and the underlying metallic surface is thus exposed. These findings are consistent with previous studies on the oxidation characteristics of Hf-based alloys, which have reported a similar tendency of oxide-layer spalling due to the formation of fine needle-like HfO_2 particles [68].

3.4. Properties of RHEAs

3.4.1. Friction and wear resistance

Fig. 6 presents the surface hardness, average friction coefficients, and wear rates of the $TZHNF_{0.5}$ RHEA in both the as-cast and oxidized states with various heating temperatures. The results indicate a general trend of increasing the surface hardness with increasing oxidation temperature, with the highest hardness value of 1146.6 Hv observed for the alloy being heated at 1000 °C. However, upon oxidation at 1200 °C, the surface of the RHEA exhibited spalling, exposing a lower degree of oxidation on the underlying alloy surface, which led to a decrease in hardness to 954.6 Hv.

In Fig. 6, the square data points represent the dry friction-wear rate (black-data points) and friction coefficient (red-data points) for different samples, while the circular data points represent the wet friction-wear rate (black-data points) and friction coefficient (red-data points) in the PBS solution. The results show that the oxidized RHEA has a greater dry-friction coefficient than the as-cast alloy due to the increased surface roughness caused by protruding oxides present on the oxidized alloy. Conversely, the wet-friction coefficient of the alloy significantly decreases, mainly resulting from the lubrication by the aqueous solution. The presence of the aqueous solution not only reduces the direct contact between the contacting surfaces but also facilitates the removal of the wear debris from the wear-track area, thereby reducing the frictional resistance and wear rate.

According to the wear rate, Eq. (2), the wear rate, W_S, of the alloy was determined:

$$W_S = \frac{\Delta W}{S \cdot N} \tag{2}$$

where ΔW represents the wear volume, S denotes the total distance of friction, and N is the normal load.

As shown in the results presented in Fig. 6, when submitted to dry friction, the RHEA exhibits a wear rate of 3.23×10^{-9} $mm^3 \cdot mm^{-1} \cdot N^{-1}$ after oxidation at 1000 °C. This wear rate is significantly lower, by two orders of magnitude, contrasted with the wear rate of the as-cast alloy. It has been reported that the wear rate of the Ti6Al4V alloy under dry friction is 2.4×10^{-7} $mm^3 \cdot mm^{-1} \cdot N^{-1}$ [67], which is two orders of magnitude larger than that of the 1000 °C-oxidized RHEA. The wear resistance of the oxidized $TZHNF_{0.5}$ RHEA is significantly higher than that of the other traditional wear-resistant biomedical implant materials, such as 4.4×10^{-8} $mm^3 \cdot mm^{-1} \cdot N^{-1}$ for the 316 L stainless steel, and 2.34×10^{-8} $mm^3 \cdot mm^{-1} \cdot N^{-1}$ for the CoCrMo alloys [67], which implies that the oxidized RHEA is promising in the application of high wear-resistant implantation instruments.

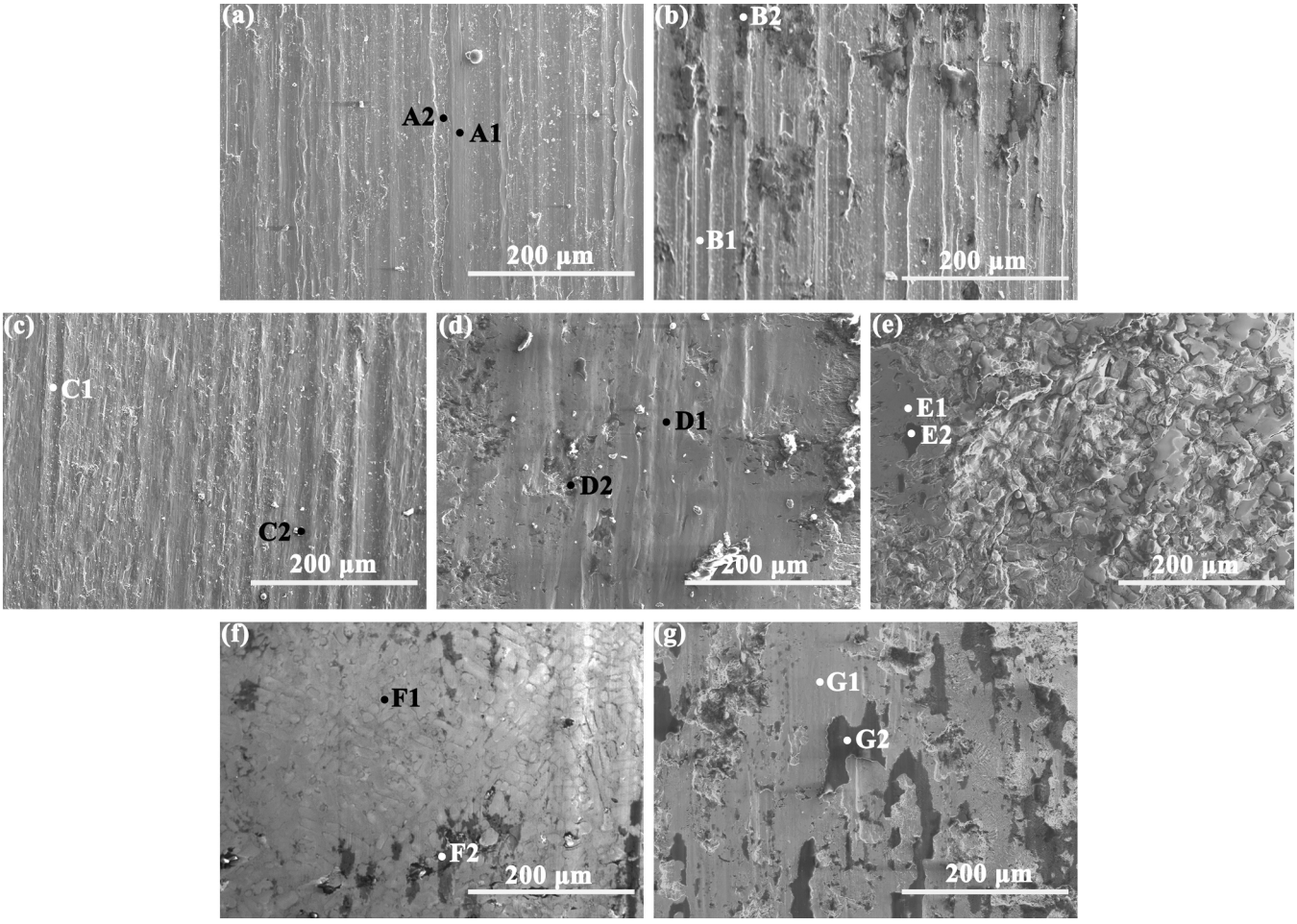

Fig. 7. Wear-scar morphologies under the dry-friction condition of the as-cast and oxidized $TZHNF_{0.5}$ RHEA: (a) as-cast state and oxidized states at (b) 300 °C, (c) 400 °C, (d) 600 °C, (e) 800 °C, (f) 1000 °C, and (g) 1200 °C.

Wet friction wear rates for different alloy samples are all lower than their corresponding dry-friction wear rates, with the lowest wet friction wear rate being recorded for the oxidized alloy being heated at 1000 °C, which is 1.54×10^{-9} $mm^3 \cdot mm^{-1} \cdot N^{-1}$. Regardless of whether the sliding occurs under dry or wet conditions, the wear rate of the RHEA after oxidation at 1000 °C is consistently the lowest, which is attributed to its highest hardness.

Fig. 7 illustrates the wear-scar morphologies under the dry-friction condition of the as-cast and oxidized $TZHNF_{0.5}$ RHEA. Fig. S2 illustrates the EDS-composition distributions of representative regions (A1-G2) corresponding to Fig. 7. In Fig. 7, it can be observed that there are distinct dark-black and light-gray contrast zones within the wear scars on the alloy surface. In Fig. 7(a-c), it can be noted that there are parallel grooves aligned with the direction of sliding within the wear-scar surfaces of the as-cast alloy and samples oxidized at 300 °C and 400 °C, suggesting that the wear mechanism of the alloy under the corresponding conditions is primarily abrasive wear. Fig. S2 demonstrate that the dark-contrast region within the wear scar of the as-cast, 300 °C-, and 400 °C-heated alloys exhibits a higher concentration of O elements, and the O content increases with increasing the oxidation temperature, revealing the oxidative-wear mechanism. In the light-gray contrast region of the alloy-wear-scar surface after oxidation at 300 °C, 400 °C, and 600 °C, the O content is comparatively small, implying that the oxide film on the alloy is thinner at the corresponding temperatures, and the oxide film is damaged and peeled off during friction, contributing to a decline in the O content.

In Fig. 7(e), severe damage in the wear scar is detected for the RHEA heated at 800 °C. The oxidized cross-sectional observation in Fig. 5(d) shows that the oxide layer has many fractures and crevices. The elevated surface O content indicates the presence of oxidative-wear mechanisms. In Fig. 7(f), the wear-scar of the RHEA after oxidation at 1000 °C exhibits a combination of dark and white contrast regions, with a notably high O content. Based on the EDS-analysis results, the dark-contrast region is identified as the Fe_2O_3 oxide, while the white contrast region is the Ti_2ZrO_6 oxide. Moreover, in Fig. 7(g), irregular pits can be observed on the alloy wear-scar surface following oxidation at 1200 °C, which progressively extend parallel to the surface with ongoing wear and eventually flake off, constituting typical morphologies of fatigue wear.

Fig. 8 displays the SEM morphologies of the wear scars of the as-cast and oxidized $TZHNF_{0.5}$ RHEAs following a wet-sliding test. Fig. S3 provides the composition distributions of the representative areas (A1-G2) corresponding to Fig. 8. Fig. 8(a-c) show that plough grooves exist on the $TZHNF_{0.5}$ RHEA surface for as-cast, 300 °C- and 400 °C-oxidized samples, although their widths are reduced when compared to the dry-friction condition. As the wet sliding processes, the RHEA undergoes reactions with the component of PBS, leading to a corrosive-wear phenomenon.

In the EDS spectra of the RHEAs under the as-cast state and oxidized conditions heating at 300 °C, 400 °C, 600 °C, and 800 °C, it can be inferred that the O content in the wear scars increases with the elevating heating temperature, which is consistent with EDS-analysis results under dry-friction conditions. Additionally, the spalling phenomenon of partial oxide films occurs on the wet-friction-wear scar of the RHEA oxidized at 600 °C, while a large area of the oxide film peeling off is found for the 800 °C-oxidized alloy, leading to a higher wear rate under

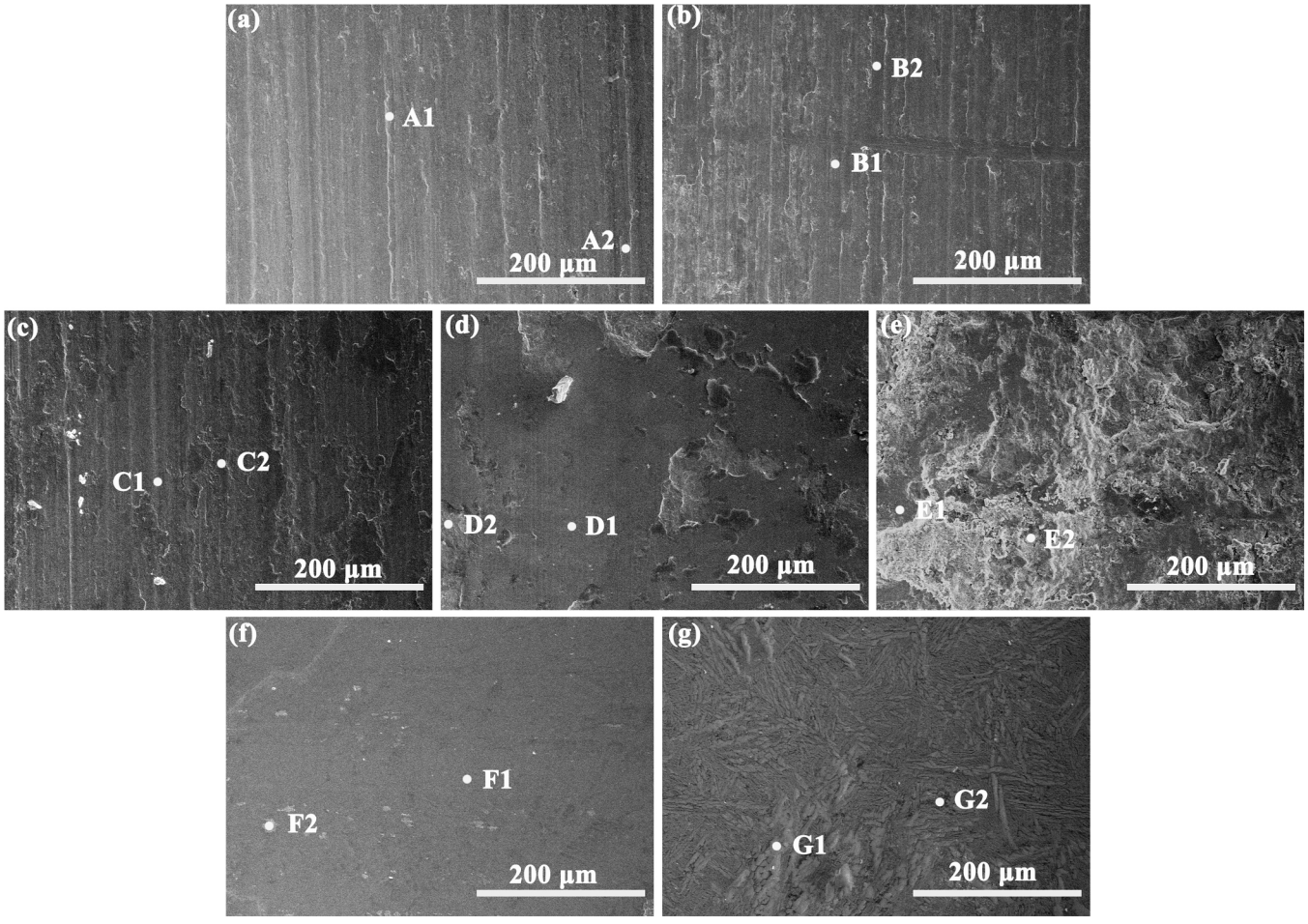

Fig. 8. SEM morphologies of the wear scar of the as-cast and oxidized $TZHNF_{0.5}$ RHEAs following a wet-sliding test: (a) as-cast state and oxidized states at (b) 300 °C, (c) 400 °C, (d) 600 °C, (e) 800 °C, (f) 1000 °C, and (g) 1200 °C.

wet-friction conditions than that under dry-friction conditions.

The $TZHNF_{0.5}$ RHEA maintains a smooth and flat surface-oxide layer after oxidation at 1000 °C, with a relatively lower O content in the alloy and no obvious corrosion-wear behavior. Additionally, for the alloy oxidized at 1200 °C, the original microstructure of the oxide layer remains on the surface after wet friction, with a relatively flat wear-scar surface and a lower wear rate under wet-friction conditions than that under dry-friction conditions.

3.4.2. Corrosion resistance

Fig. 9(a) presents the potentiodynamic-polarization curves of the as-cast and oxidized $TZHNF_{0.5}$ RHEA at 300 °C, 400 °C, and 1000 °C, together with the Ti6Al4V alloy, with the associated electrochemical parameters tested in the PBS solution summarized in Table 1. Due to the delamination and unevenness of the surface-oxide layer, electrochemical-polarization experiments were not conducted for the $TZHNF_{0.5}$ RHEA oxidized at 600 °C, 800 °C, and 1200 °C. The $TZHNF_{0.5}$ RHEA exhibits a superior corrosion potential relative to the Ti6Al4V alloy, signifying that the passivation film developed in the PBS solution possesses elevated stability. In particular, the RHEA oxidized at 1000 °C demonstrates the highest corrosion potential in the PBS solution, amounting to - 0.21 V. The corrosion current density of the $TZHNF_{0.5}$ RHEA decreases with increasing the oxidation temperature, attaining the lowest value of 1.46×10^{-7} A·cm^{-2} after oxidation at 1000 °C. This value is considerably smaller than that of the Ti6Al4V, denoting a reduced corrosion rate in the PBS solution. Furthermore, the passivation-current density of the oxidized RHEA is substantially smaller

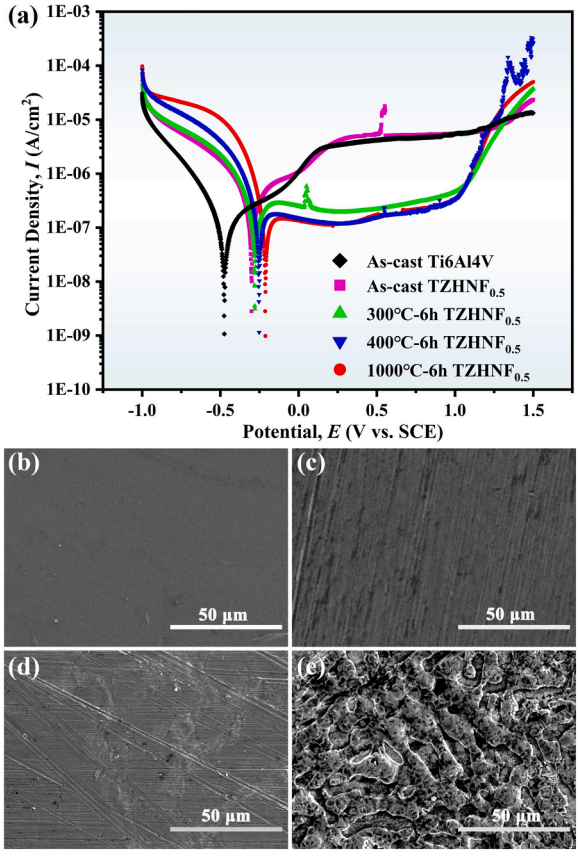

Fig. 9. (a) Potentiodynamic-polarization curves of the as-cast and oxidized $TZHNF_{0.5}$ RHEA at 300 °C, 400 °C, and 1000 °C, together with the Ti6Al4V alloy in the PBS solution, (b-e) SEM morphologies of the as-cast $TZHNF_{0.5}$ RHEA and the corresponding alloy oxidized at 300 °C, 400 °C, and 1000 °C subsequent to electrochemical experiments: (b) as-cast state, (c) 300 °C, (d) 400 °C, (e) 1000 °C.

Table 1
Electrochemical parameters of the as-cast and oxidized $TZHNF_{0.5}$ RHEA at 300 °C, 400 °C, and 1000 °C, together with the Ti6Al4V alloy.

Alloy	Condition	E_{corr} /V	i_{corr} /A·cm^{-2}	i_{pass} /A·cm^{-2}
$TZHNF_{0.5}$	As-cast	- 0.30	2.80×10^{-7}	5.65×10^{-6}
	300 ℃−6 h	- 0.28	2.43×10^{-7}	3.11×10^{-7}
	400 ℃−6 h	- 0.25	1.68×10^{-7}	1.94×10^{-7}
	1000 ℃−6 h	- 0.21	1.46×10^{-7}	1.57×10^{-7}
Ti6Al4V	As-cast	- 0.47	1.70×10^{-7}	4.97×10^{-6}

than that of the as-cast RHEA and Ti6Al4V, reaching the lowest value of 1.57×10^{-7} A·cm^{-2} post-oxidation at 1000 °C, implying that the oxidation heat treatment enhances the passivation film stability.

Fig. 9(b-e) display SEM morphologies of the as-cast $TZHNF_{0.5}$ RHEA, and the corresponding alloy oxidized at 300 °C, 400 °C, and 1000 °C subsequent to electrochemical experiments. Through the comparative analysis of the images, no evident pits of corrosion can be observed on the polarized alloy, thereby suggesting the absence of pitting corrosion and the maintenance of sound structural integrity on the alloy surface.

Fig. 10 illustrates the XPS full spectra and narrow scan spectra of individual alloying elements for the as-cast and PBS-immersed $TZHNF_{0.5}$ RHEA, with the resulting XPS composition analysis results compiled in Table 2. As depicted in Fig. 10(a), all alloy samples manifest the presence of C 1 s, Ti 2p, Hf 4 f, Nb 3d, Fe 2p, Zr 3d, and O 1 s peaks in the XPS full spectra of the free surfaces. Examining the narrow scan spectra of Ti 2p, Hf 4 f, Nb 3d, Fe 2p, Zr 3d, and O 1 s in Fig. 10(a-g), it can be observed that the structures corresponding to these elements are consistent under the four different conditions, and the intensity of the alloy-element peaks significantly increases after immersion.

In Fig. 10(c) and (d), a notable decrease in the intensities of Zr^{4+} and Hf^{4+} before and after oxidation can be observed, while a significant enrichment of Ti^{4+}, Nb^{5+}, Fe^{3+}, and O^{2-} is evident in the oxidized alloy. The pronounced increase in the content of Fe^{3+} and O^{2-} on the alloy surface implies the creation of surface Fe oxides, which corresponds to the presence of Fe_2O_3 as a protruding oxide in the surface morphology and composition analysis of the alloy. Furthermore, the relatively increased content of Ti^{4+} and Nb^{5+} in the outer layer of the alloy-oxide layer also contributes to the improvement of the anticorrosion property. Particularly, the strong passivation ability of Ti itself enhances the surface film by forming a corrosion-resistant TiO_2 oxide through the adsorption of negative ions, such as OH^- or O^{2-} [58,69]. Concurrently, the addition of Nb^{5+} increases the number of O^{2-}, compensating for the anionic vacancy in the passivating film, leading to a reduction in film defects and ultimately resulting in a more stable passivating film [70].

In Fig. 10(g), the O 1 s spectral peaks observed on the alloy surface both in the as-cast state and after immersion can be attributed to oxygen present in metal oxides or hydroxides, as well as oxygen in the form of bound water (H_2O) [71]. As the RHEA is heated at 1000 °C, the O on the oxidized and immersed alloys predominantly transitions to O^{2-}. Consequently, the $TZHNF_{0.5}$ RHEA demonstrates exceptional corrosion resistance after oxidation at 1000 °C.

3.4.3. Biological activity

Fig. S4 displays SEM images and EDS mapping of the sample surfaces of the $TZHNF_{0.5}$ RHEA being immersed in SBF for 14 days: (a) as-cast, (b) oxidized at 1000 °C, and (c) oxidized at 1000 °C and then surface grinding. As shown in Fig. S4(a), a surface film forms on the alloy surface after casting, with some white particles (indicated by red circles) distributed on the surface film, which are identified as reaction products rich in Ca and P elements through the EDS analysis. Cracks are found on the surface film. Fig. S4(a1) shows numerous white needle-like reaction products covering the alloy surface, forming a porous surface film, which is confirmed to be hydroxyapatite (HAP) through composition analysis.

Fig. S4(b) illustrates that there are numerous protrusions with a well-

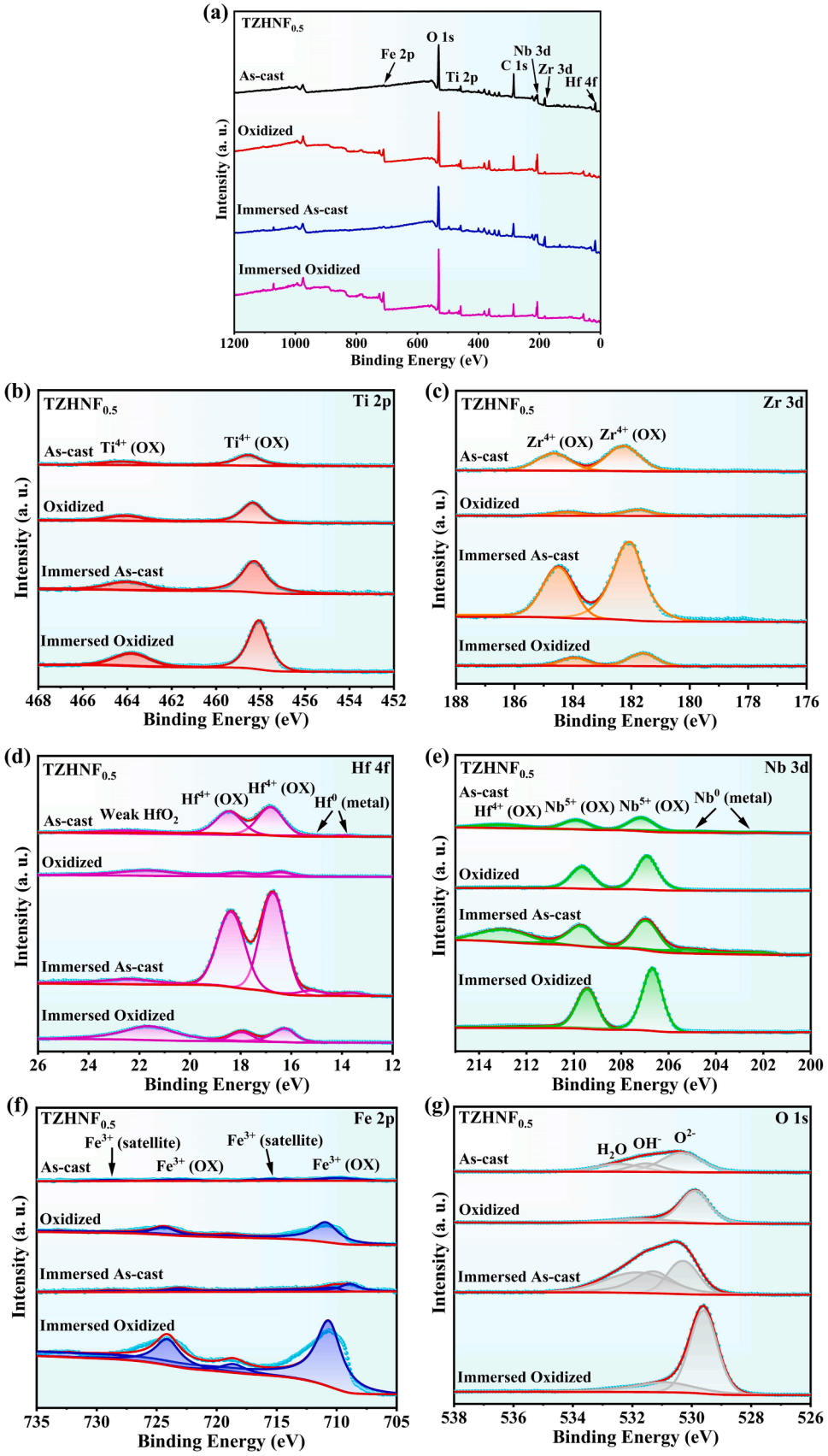

Fig. 10. (a) XPS full spectra and narrow scan spectra of individual alloying elements for the as-cast and PBS-immersed $TZHNF_{0.5}$ RHEA. (b) Ti, (c) Zr, (d) Hf, (e) Nb, (f) Fe, and (g) O.

Table 2
XPS composition-analysis results of the as-cast and PBS-immersed $TZHNF_{0.5}$ RHEA.

Element (at%)		Alloy			
		as-cast	1,000 °C-6 h	Immersed as-cast	Immersed 1,000 °C-6 h
Ti 2p	Ti^{4+}	7.49	10.3	5.36	5.91
Zr 3d	Zr^{4+}	7.25	1.53	5.03	0.96
Hf 4 f	Hf^{4+}	6.64	1.17	5.13	0.64
	Hf^{0}	0.22	-	0.29	-
Nb 3d	Nb^{5+}	6.82	13.39	5.07	6.19
	Nb^{0}	0.28	-	1.13	-
Fe 2p	Fe^{3+}	2.50	17.46	2.83	16.37
O 1 s	O^{2-}	38.02	43.97	22.29	53.93
	OH^{-}	16.87	12.18	23.15	16.00
	H_2O	13.12	-	29.71	-

defined and dense "glaze-like" surface film present on the alloy surface of the 1000 °C-heated and SBF-immersed $TZHNF_{0.5}$ RHEA. Interestingly, similar to the previous case, numerous white-particle-reaction products (indicated by red circles) could also be observed in the surface film. The SEM picture in Fig. S4(b1) clearly shows that numerous white needle-like hydroxyapatites (HAP) are "embedded" within the surface-oxide film. In contrast to the preceding two situations, as seen in Fig. S4(c), grinding removes the protrusive oxide, resulting in a considerable reduction in the quantity of white-particle deposits on the surface alloy. Notably, as depicted in Fig. S4(c1), no well-defined and dense "glaze-like" surface film is formed on the alloy surface, but rather, numerous white needle-like HAPs are present, giving rise to a porous surface film.

It is well-known that the Ca and P elements are the primary constituents of HAP, and thus, the EDS elemental analysis was conducted on the alloy surface, as presented in Figs. S4(a-c). Table S1 exhibits the EDS elemental-distribution data for the as-cast and oxidized $TZHNF_{0.5}$ RHEAs after immersion in SBF for 14 days. As observed in Figs. S4(a-c), the alloy-sample surface after being heated at 1000 °C exhibits a Ca/P ratio approaching 1.67, which is characteristic of hydroxyapatite, indicating good bioactivity. The protrusions removed through surface grinding are primarily identified as Fe_2O_3, resulting in a decrease in the Fe content on the alloy surface and a corresponding decline in the concentrations of Ca and P elements. This trend demonstrates that the Fe element in the RHEA helps make a hydroxyapatite surface layer [72]. Moreover, the Fe component has been found to expedite the growth of hydroxyapatite on the alloy surface. It is known that Fe is a good carrier for the constant dissolution of Fe^{3+}, which can hinder the entry of mineral ions, thereby showing significant bioactivity [73].

4. Discussion

In the present work, the effects of various oxidation temperatures on the mechanical performance, antiwear and anticorrosion qualities, and biological activity of the $TZHNF_{0.5}$ RHEA was studied. It is illustrated that the $TZHNF_{0.5}$ RHEA exhibits a much slower oxidation velocity at 1000 °C than that found at 800 °C and 1200 °C. After oxidation at 1000 °C, a dense and stable surface layer form, which exhibits excellent comprehensive performance. In order to elucidate the reasons behind the outstanding antioxidant properties of the $TZHNF_{0.5}$ RHEA, we discussed the surface-structural evolution and oxidation mechanism of the $TZHNF_{0.5}$ RHEA heated at 1000 °C.

4.1. Composition and oxidation resistance of RHEA's 1000 °C oxide layer

The "abnormal" oxidation behavior of the $TZHNF_{0.5}$ RHEA at 1000 °C is closely associated with the microstructure of the oxide layer [74,75]. As shown in the cross-sectional morphologies of the oxidized alloy in Fig. 5, the RHEA exhibits four distinct zones with varying microstructures from the surface to the core. The oxide layer itself encompasses two distinct regions with differing microstructures, while there are two additional zones with unique microstructures located between the oxide layer and the metallic matrix. Through grinding the alloy and conducting phase analysis and microstructure observations on each layer's surface, our study provides insights into the oxidation process of the $TZHNF_{0.5}$ RHEA at 1000 °C. Fig. 11 depicts the XRD patterns of the surface and four different regions of the $TZHNF_{0.5}$ RHEA as heated at 1000 °C. Among them, Figs. 12(b-b1), (c-c1), (d-d1), and (e-e1) are magnified cross-sections and surface images of Layer I, Layer II, Layer III, and Layer IV in Fig. 12(a). Table 3 shows the EDS analysis results of the four surface regions corresponding to Fig. 12. From the outermost to the innermost regions, this study determines the oxidation process of the $TZHNF_{0.5}$ RHEA heated at 1000 °C based on the characteristics of phases in each layer.

In the XRD pattern of Layer I, there are Fe_2O_3, Ti_2ZrO_6, and $(TiZrHfNb)O_2$ oxides present. Compared to the surface XRD, the intensity of the Fe_2O_3 diffraction peak has decreased. From the analysis of Figs. 12(b)-(b1) and the EDS analysis of the corresponding region in Fig. 12(b1), the white contrast cellular region is identified as the BCC phase and the complex oxide $(TiZrHfNb)O_2$, while the fine dendritic region is determined to be the Laves phase. The black-contrast region is attributed to the Fe_2O_3 phase, and the dark-contrast region corresponds to the Ti_2ZrO_6 phase. In the XRD pattern of Layer II, there are primarily HfO_2 oxides present, with lower diffraction peaks for the BCC and the Laves phases. From the analysis of Figs. 12(c-c1), numerous fine needle-like substances can be detected in the cellular dendrites from the top to bottom in the section, with a surface microstructure that is similar to the matrix. Due to the presence of these fine needle-like substances in the cellular dendrites, there are evident white dot-like areas observed. The corresponding EDS analysis identifies the light-colored cellular contrast area as the complex oxide $(TiZrHfNb)O_2$, with the white dot-like area being attributed to the HfO_2 oxide, which is in the form of fine needles and is consistent with the previously reported morphology of the HfO_2 phase by Ouyang et al. [68]. The dark-contrast area is identified as the Laves phase. The light-contrast cellular dendrites are rich in Nb, while the dark-contrast fine dendrites are predominantly composed of Fe.

In the XRD pattern of Layer III, the BCC and Laves phases are predominantly present. As illustrated in Fig. 12(a), Layer-III functions as a transitional layer situated between the substrate and the oxide layer. Examining Figs. 12(d-d1), it can be observed that the surface

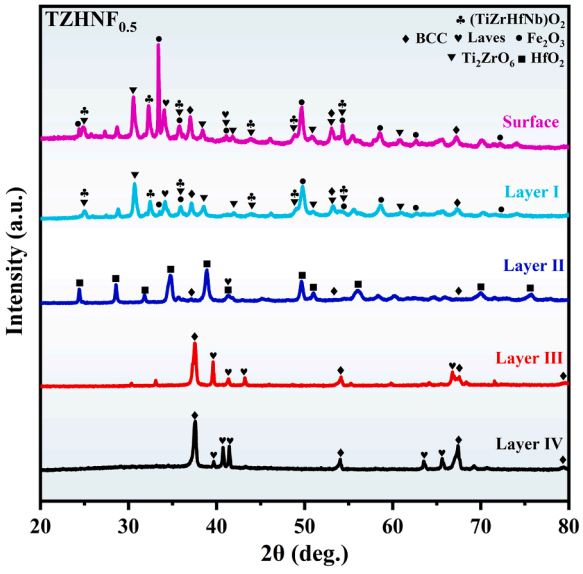

Fig. 11. XRD patterns of the surface and four different regions of the $TZHNF_{0.5}$ RHEA as heated at 1000 °C.

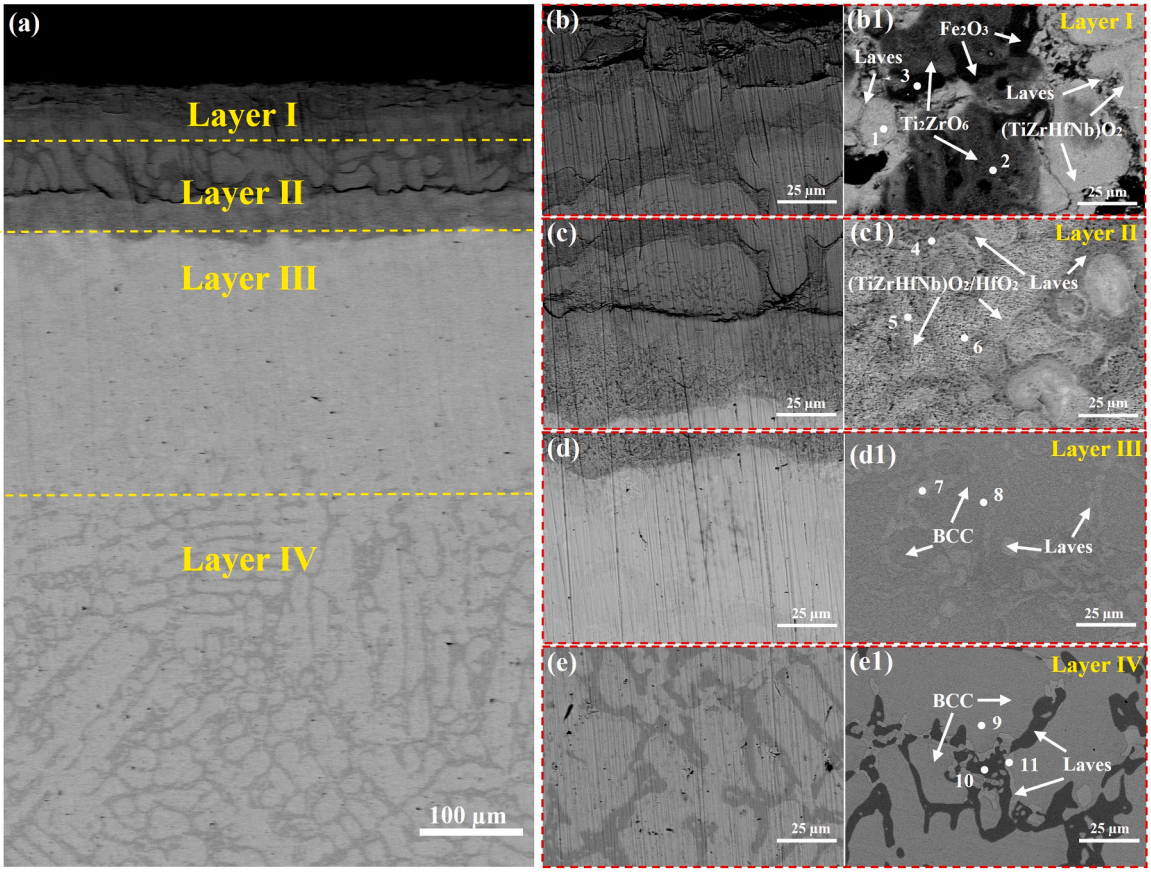

Fig. 12. (a) Cross-sectional morphology of the $TZHNF_{0.5}$ RHEA as heated at 1000 °C. (b-b1), (c-c1), (d-d1), and (e-e1) are magnified cross-sections and surface images of Layer I, Layer II, Layer III, and Layer IV in Fig. 12(a).

Table 3
EDS analysis results of the four surface regions corresponding to Fig. 12.

Position		Element (at%)					
		Ti	Zr	Hf	Nb	Fe	O
Layer I	1	12.50	16.09	11.92	15.51	3.24	40.73
	2	17.86	7.78	3.48	17.42	6.97	46.48
	3	3.88	1.60	0.28	0.47	29.85	65.32
Layer II	4	17.87	15.73	12.29	5.70	16.18	32.22
	5	12.55	16.37	11.91	29.76	0.23	29.17
	6	19.61	16.86	7.48	18.18	12.54	25.35
Layer III	7	18.30	18.57	26.45	4.69	31.99	-
	8	26.17	26.50	17.43	27.45	2.45	-
Layer IV	9	23.04	27.60	25.78	21.04	2.53	-
	10	23.82	17.12	16.63	13.22	29.22	-
	11	16.75	17.92	28.71	4.30	32.32	-

microstructure is analogous to the substrate, while the dendritic and interdendritic structures of this layer are more homogeneous. In particular, through the EDS analysis, the darkly contrasting dendritic region is identified as the BCC phase, while the lightly contrasting interdendritic region is determined as the Laves phase. Similar to the as-cast alloy, the dendrites and interdendritic regions exhibit Nb-rich and Fe-rich phenomena, respectively. However, what distinguishes this layer is the emergence of Ti-rich and Hf-rich phenomena in the dendrites and interdendritic regions. In Fig. 12(a), Layer IV constitutes the substrate layer, comprising both the BCC and Laves phases, which aligns with the microstructure of the as-cast alloy. Through the examination of Figs. 12 (a) and (e-e1), it can be observed that the microstructure is further refined. Combining EDS analysis, the light-contrast dendritic region is the BCC phase, while the dark-contrast interdendritic region is the Laves phase.

In order to further explore the microstructural evolution of the surface oxide layer after oxidation, TEM samples of as-cast and oxidized $TZHNF_{0.5}$ RHEA at 1000 °C for 6 h were prepared using focused ion beam (FIB) technology. Fig. 13(a) shows the FIB sampling position of the as-cast $TZHNF_{0.5}$ refractory high entropy alloy, which is located at the boundary region between dendrites and interdendritic regions. Fig. 13 (a1) and (a2) are SEM images of the FIB-prepared samples of the as-cast $TZHNF_{0.5}$ RHEA. Fig. 13(b) illustrates the HAADF image and the corresponding elemental composition distribution of the enlarged area in the red box in Fig. 13(a2). From Fig. 13(b), it can be observed that the region 1 corresponds to the position of the interdendritic Laves phase, where Fe element enrichment occurs, while the region 2 corresponds to the position of the dendritic BCC phase, where Nb element enrichment takes place. In addition, it can also be found that a small amount of BCC phase crystals are distributed in the Laves phase.

Fig. 13(c) displays the bright-field TEM image of the as-cast $TZHNF_{0.5}$ RHEA in the enlarged area of the red box in Fig. 13(a2), as well as the HRTEM and selected area electron diffraction (SAED) images corresponding to different regions. Through the analysis of region A in Fig. 13(c), it can be found that the lattice spacing in the yellow box area of Fig. 13(A1) is 0.2247 nm, which is basically consistent with the $(10\bar{1}3)$ crystal plane of the hexagonal Laves phase. Meanwhile, the SAED image in Fig. 13(A2) further confirms that there is the Laves phase along the $[1\bar{2}1\bar{3}]$ crystal zone axis in this region. In addition, the lattice spacing in the blue box area of Fig. 13(A1) is 0.1778 nm, which is basically consistent with the (112) crystal plane of the orthorhombic BCC phase. The SAED image in Fig. 13(A3) further confirms that this region is the BCC phase along the [001] crystal zone axis. The analysis results of region B in Fig. 13(c) demonstrate that the BCC phase structure is

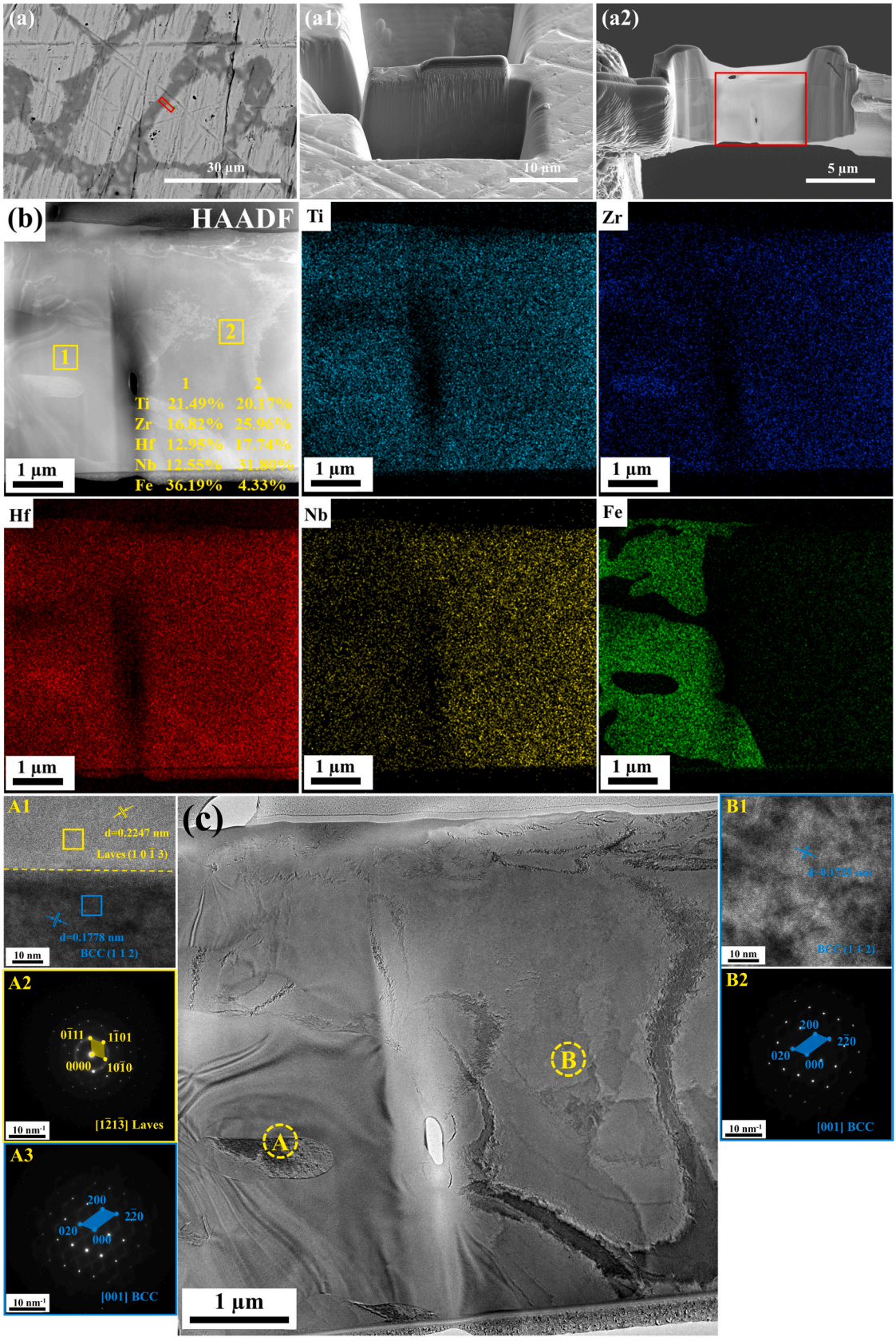

Fig. 13. (a-a1) The SEM images of the sampling location and morphologies during the preparation process for the as-cast $TZHNF_{0.5}$ RHEA TEM sample prepared by focused ion beam (FIB) technology. (b) HAADF image of the enlarged area in the red frame of Fig. 13(a2) and the elemental mapping images of Ti, Zr, Hf, Nb, and Fe corresponding to Fig. 13(b); (c) TEM bright field image of the red area in Fig. 13(a2), as well as the HRTEM and SAED images corresponding to different regions.

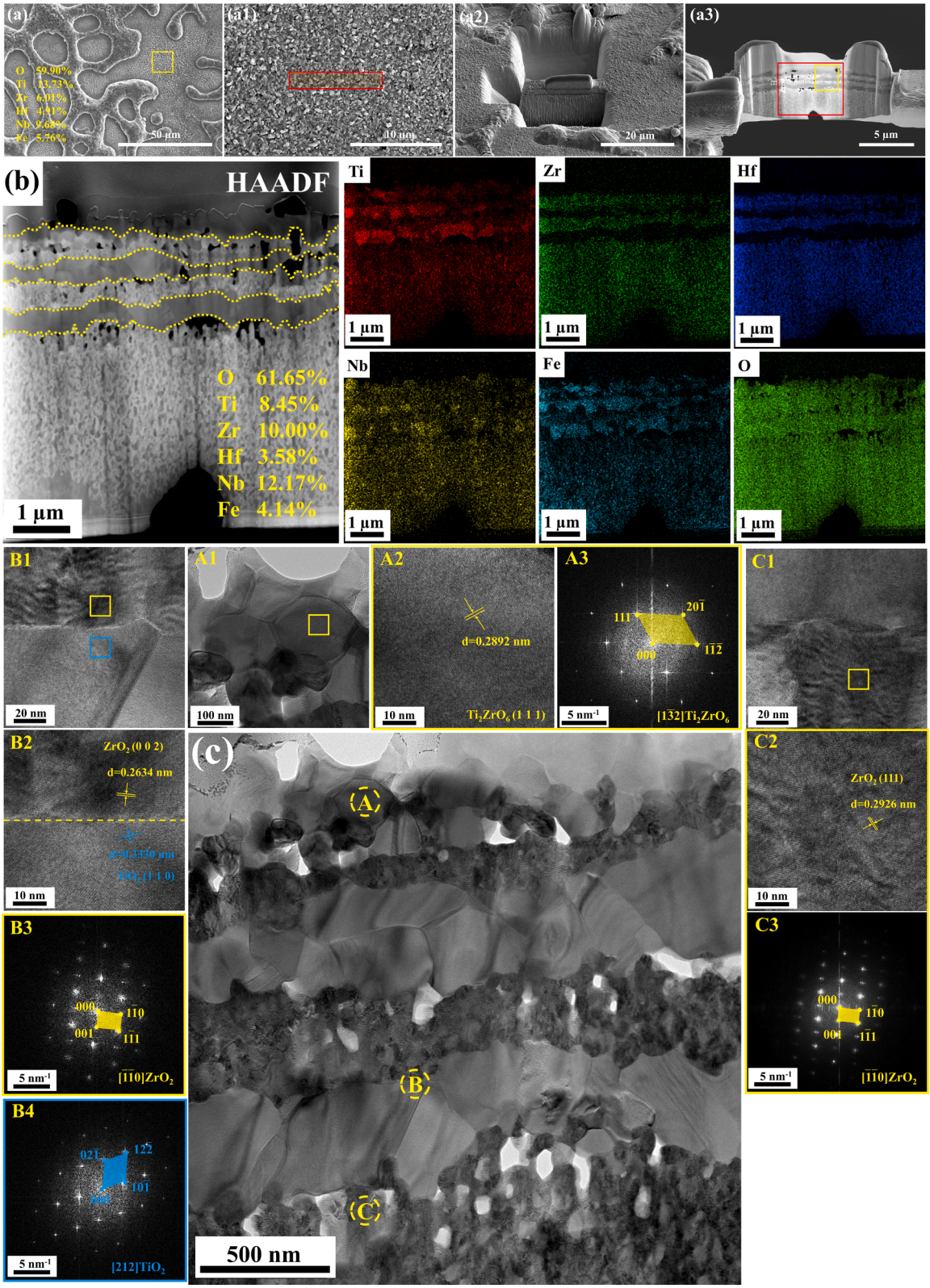

Fig. 14. (a-a3) The preparation of a TEM sample of the TZHNF0.5 RHEA oxidized at 1000 °C for 6 h using FIB technology. (b) HAADF image of the magnified area within the red box in Fig. 14(a3), along with the corresponding elemental mapping images of Ti, Zr, Hf, Nb, Fe, and O elements. (c) TEM bright-field image of the yellow area in Fig. 14(a3), accompanied by HRTEM and SAED images corresponding to different regions.

consistent with that in region A.

Fig. 14(a) illustrates the SEM image of the surface morphology of the $TZHNF_{0.5}$ RHEA after oxidation treatment at 1000 °C for 6 h. From the figure, it can be seen that the surface of the oxidized $TZHNF_{0.5}$ RHEA exhibits two different contrast regions, which consist of the dark-contrast island-like protruding region and the gray-white-contrast flat region. The EDS analysis results of the flat region are also listed in Fig. 14 (a). Fig. 14(a1) displasys the FIB sampling area located in the flat region with gray-white contrast, which corresponds to the position of the BCC phase in the as-cast sample. After oxidation heat treatment, the surface is densely packed with nanoparticles, which are mainly composed of Ti_2ZrO_6. Fig. 14(a2) demonstrates the SEM image of the TEM sample preparation process using the FIB technique. Fig. 14(a3) shows the SEM image of the TEM thin film specimen prepared using the FIB sampling process. Fig. 14(b) presents the HAADF image of the red box area of the TEM sample referring to Fig. 14(a3) and the distribution of Ti, Zr, Hf, Nb, Fe, and O elements in the corresponding area. From Fig. 14(b), it can be observed that the outermost surface of the oxide layer is covered with a layer of nanoparticles, and the interior of the oxide layer exhibits two regions with dark and bright contrasts, with the dark-contrast region distributed in a layered manner within the bright-contrast matrix. Combining the elemental distribution in Fig. 14 (b), it can be seen that Ti and Fe elements are enriched in the dark-contrast region, while Zr and Hf elements are enriched in the bright-contrast region, and Nb and O element oxides are uniformly distributed throughout the oxide layer. Based on the EDS analysis results and the analysis of the microstructure morphology of the cross-section of the as-cast $TZHNF_{0.5}$ RHEA in Fig. 13, it is known that in the cross-sectional area of the as-cast alloy, the BCC phase and Laves phase are interlaced in a layered manner. Therefore, in the microstructure morphology of the cross-section of the oxidized $TZHNF_{0.5}$ RHEA in Fig. 14 (b), the dark-contrast region and bright-contrast region are oxides formed by the Laves phase BCC phase in the as-cast alloy through O diffusion reaction, respectively.

Fig. 14(c) presents the TEM bright-field image of the surface oxide layer of the $TZHNF_{0.5}$ RHEA after oxidation at 1000 °C for 6 h, along with HRTEM and SAED images corresponding to different regions. The bright-field image corresponds to the magnified area within the yellow box in Fig. 14(a3). From the HRTEM image in Fig. 14(A2), the lattice spacing of this crystalline phase is determined to be 0.2892 nm, which corresponds to the interplanar spacing of the orthorhombic oxide Ti_2ZrO_6 (111) plane, consistent with the results from literature analysis [76]. The SAED pattern in Fig. 14(A3) further confirms that this region exhibits the electron diffraction pattern of Ti_2ZrO_6 along the $[\bar{1}13]$ zone axis. In Fig. 14(B1), the HRTEM images of the regions within the yellow and blue boxes reveal lattice spacings of 0.2634 nm and 0.3330 nm, respectively, which correspond to the orthorhombic oxide ZrO_2 (002) and TiO_2 (110) planes. The corresponding SAED patterns in Fig. 14(B3) and (B4) further validate the presence of ZrO_2 along the $[\bar{1}\bar{1}0]$ zone axis and TiO_2 along the [212] zone axis in this region. Analysis of the corresponding region C in Fig. 14(c) also yields the orthorhombic oxide ZrO_2. In summary, ZrO_2 and TiO_2 possess similar crystal structures (orthorhombic system, simple lattice) and have comparable ionic radii of Zr^{4+} (0.72×10^{-10} m) and Ti^{4+} (0.68×10^{-10} m) [77], facilitating their reaction to form the Ti_2ZrO_6 oxide. The nanoscale particles of Ti_2ZrO_6 formed on the surface of the oxide layer are intact and stable, effectively inhibiting oxygen ingress and reducing the oxidation rate. The formation of ZrO_2 and TiO_2 oxides within the internal structure of the oxide layer enhances its hardness, thereby improving wear resistance. Additionally, the Ti_2ZrO_6, ZrO_2, and TiO_2 oxides formed on the alloy surface exhibit excellent chemical stability, significantly enhancing the corrosion resistance of the alloy.

Developing a dense and stable oxide layer is essential for HEAs to possess good oxidation resistance. However, the formation of stable oxide layers in HEAs is influenced by numerous factors, with the internal stress being a critical factor. In Fig. 4(e-g), the oxidation layers of the $TZHNF_{0.5}$ RHEA experience destructive spalling due to the action of internal stresses at 800 °C and 1200 °C, whereas a dense and stable oxide layers form at 1000 °C. To clarify the oxidization behavior, the Pilling-Bedworth Ratio (PBR) is introduced to evaluate the influence of each oxide on internal stresses [78,79], and the volume expansion caused by oxidation is deduced through Eq. (3) [80–82]:

$$PBR = \frac{V_{oxide}}{V_{ally}} = \frac{\rho_a M_o}{x \rho_o A_a} \tag{3}$$

where ρ_o is the density of the oxide, ρ_a is the density of the alloy at room temperature, M_o represents the molar mass of the oxide, A_a stands for the effective molar mass of the alloy, and x is the number of metal atoms of corresponding oxides.

The PBR is used to evaluate the antioxidation performance of an oxide layer. The value of PBR below 1 represents a low protective property with the oxide layer that cannot fully cover the metal surface. When the PBR is between 1 and 2, the oxide layer can completely cover the alloy surface, offering optimal protective properties [83]. However, when the PBR exceeds 2, the oxide layer may develop excessive compressive stresses, leading to its rupture or decomposition, thereby reducing the protective effectiveness of the oxide film [84,85].

According to Eq. (3), the $TZHNF_{0.5}$ RHEA has an A_a value of 94.97 g, and the PBR values of the primary oxides in the oxide layer are listed in Table 4. Notably, the PBR value of Nb_2O_5 reaches 2.60, despite the fact that Fe_2O_3 has a lower PBR. Even so, the oxide film on the alloy surface still experiences significant stress and peeling at 800 °C. Furthermore, employing the methodology described in Reference [86], the PBR value of the composite oxide, Ti_2ZrO_6, is calculated to be 1.71, suggesting that it is more likely to form an oxide film with superior protective properties. Overall, the analysis based on the PBR values of various oxides is consistent with the experimental observations.

Interestingly, the PBR value of HfO_2 is below 2, which would normally facilitate the formation of protective films. However, substantial amounts of HfO_2 were observed to detach from the alloy surface at 1200 °C. To account for this discrepancy, this study delves deeper into the mechanism behind the development of voids and fractures in the surface layer. The primary cause of void formation in the $TZHNF_{0.5}$ RHEA after oxidation at 1200 °C lies in the clustering and segregation of HfO_2 at the interface between the oxide and metallic matrix. The volumetric expansion incurred during the growth of HfO_2 generates stresses at the oxide/metal interface [87]. The heterogeneous distribution of HfO_2 in the $(TiZrHfNb)O_2$ results in stress concentration. Moreover, the presence of stress also impacts the spalling of the oxide layer, as indicated in Fig. 5(d) and (f).

Ouyang et al. discovered that the dense surface layer exhibits large-scale elemental segregation, where the Hf element in the form of HfO_2 is found to exist separately in certain regions of the oxide layer, disrupting the original overall structure of the composite oxide, leading to the precipitation of various types of oxides and a sharp increase in the oxygen diffusivity [68]. Sheikh et al. observed that the HfO_2-oxide distribution in the sub-oxide layer is chaotic, and interlaces with each other, resulting in an extremely non-dense alloy oxide layer, which is prone to cracking and peeling off the oxide layer [66]. Therefore, the dispersion of HfO_2 in the surface is a pivotal factor, exerting a profound impact on the antioxidant property.

In order to obviate the influence of HfO_2 on the cracking of the oxide layer, we have developed a Hf-free Ti-Zr-Nb-Fe titanium alloy in subsequent endeavors. Employing an appropriate thermal oxidation process, we have achieved a complete, compact, and crack-free oxide layer.

Table 4
PBR values of the primary oxides in the oxide layer of the $TZHNF_{0.5}$ RHEA.

	Nb_2O_5	Fe_2O_3	Ti_2ZrO_6	HfO_2	TiO_2	ZrO_2
PBR	2.60	1.33	1.71	1.90	1.64	1.84

The pertinent findings will be documented in a separate publication.

4.2. Oxidation mechanism of RHEAs at 1000 °C

Based on the aforementioned findings, the $TZHNF_{0.5}$ RHEA undergoes oxidation at 1000 °C, resulting in the formation of four distinct structural layers and an oxide layer with outstanding antioxidant properties. A further investigation into the oxidation mechanism reveals that the development of the oxide is dependent on the initial chemical absorption and reactions during the oxidation process, with its composition determined by the diffusion of solutes from the grain boundaries to the alloy surface [88,89]. In the growth stage of the oxide film, oxygen and metal ions further oxidize through the internal and external migration. However, a slight increase in the alloy-oxidation weight during the later process of oxidation may be associated with the dense surface-oxide film.

According to the thermodynamic theory, the standard Gibbs free energy (ΔG^0) is an essential thermodynamic parameter. Under specific conditions, the more negative ΔG^0 value of a metal oxide, the greater the possibility and tendency of oxidation reactions, the stronger the metal's ability to bond with oxygen, and the higher the stability of the formed oxide. The oxidation-reaction equations of the primary elements of the $TZHNF_{0.5}$ RHEA and the corresponding ΔG^0 values are illustrated in Fig. 15. In this study, under standard conditions and using the consumption of 1 mol. of oxygen as a reference, the ΔG^0 values of various oxides are calculated. At 1000 °C, the ΔG^0 values of various oxides are described as follows:

$$\Delta G^0Fe_2O_3 > \Delta G^0Nb_2O_5 > \Delta G^0TiO_2 > \Delta G^0ZrO_2 > \Delta G^0HfO_2$$

Therefore, at 1000 °C, the HfO_2 oxide has a higher tendency to form than other metal oxides, followed by ZrO_2, TiO_2, Nb_2O_5, and Fe_2O_3 oxides. However, in this study, the corresponding oxides did not form in the oxide layer, with mainly Fe_2O_3 and Ti_2ZrO_6 oxides present, among which the HfO_2 oxide is located between the oxide layer and the substrate. This is primarily due to kinetic considerations, based on the Arrhenius Equation [90].

$$D = D_0 e^{-\frac{Q}{RT}} \tag{4}$$

where D denotes the diffusion coefficient, D_0 represents the pre-expansion component, Q defines the diffusion-activation energy, and T embodies the diffusion temperature. In this equation, D_0 and Q are constants that refer to the alloy composition. R is a gas constant, which is 8.314 J/ (mol·K).

According to the diffusion theory reported in Reference [91], high-melting-point elements exhibit strong atomic-bonding forces and large diffusion-activation energies, which results in smaller diffusion coefficients. Conversely, the low density of BCC structure enhances the diffusion coefficient of these elements. Consequently, Zr, Ti, and Fe elements exhibit significantly faster diffusion rates than Nb and Hf elements during oxidation processes. Moreover, on the surface, preferential oxidation occurs for Zr and Ti elements in their BCC phase. As demonstrated in Fig. 15, thermodynamically, TiO_2 and ZrO_2 are more stable than Fe_2O_3 during the earliest phases of heating at 1000 °C, and are therefore, expected to form preferentially. In this study, TiO_2 and ZrO_2 share similar crystal structures and cation radii, leading to the formation of the Ti_2ZrO_6 ($2TiO_2$-ZrO_2) compound. During the formation of continuous Ti_2ZrO_6 oxide films, metal and oxygen ions undergo oxidation via diffusion within the oxide layer, and their respective diffusion coefficients represent one of the primary factors governing the oxidation rate.

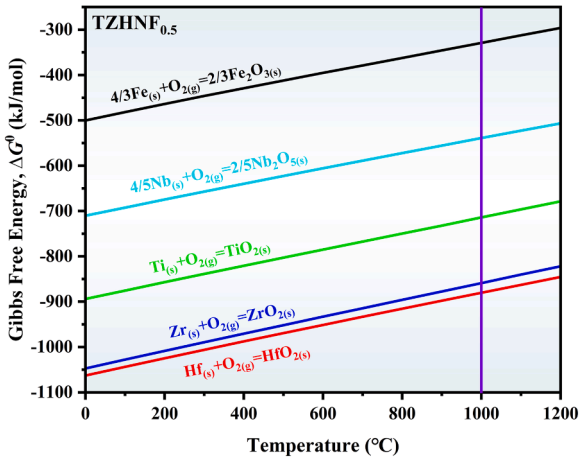

Fig. 15. Oxidation-reaction equations of the primary elements of the $TZHNF_{0.5}$ RHEA and the corresponding ΔG^0 values.

Wagner et. al reported that the parabolic oxidation rate constant, K_W, is directly associated with the oxidation rate rather than the thermodynamic stability of metal-oxide phases [92]. As demonstrated in Reference [93], although TiO_2 has better thermodynamic stability than Fe_2O_3, its K_W value is an order of magnitude lower. Consequently, the Fe_2O_3 oxide exhibits a notably higher oxidation rate in comparison with the Ti_2ZrO_6 oxide. Fe ions are able to rapidly diffuse towards the alloy surface through the Laves phase, forming the protruding oxide Fe_2O_3 by combining with O ions. As a result, the rapid formation of Ti_2ZrO_6 and Fe_2O_3 oxides during the initial stages of oxidation leads to a rapid increase in the weight. Once a complete surface-oxide layer is developed, the oxidation reaction shifts from being directly between the metal and oxygen to being controlled by the metal cation outward diffusion and oxygen ions inward diffusion through the oxide layer, leading to a little weight gain.

The results presented in Fig. 5(g) and Table 3 suggest a gradual decrease in the concentration of the O element from the outer to the inner regions of the oxidized layer, while the Nb element is primarily present in the form of $(TiZrHfNb)O_2$ composite oxides, with no evidence of Nb_2O_5 oxides in the XRD pattern shown in Fig. 11. This observation coincides with the low diffusion coefficient of Nb, which results in a depletion of O ions in Layer I due to their consumption by Ti, Zr, and Fe ions, leading to the formation of a dense and continuous Ti_2ZrO_6 oxide film. A limited amount of O ions diffuses into Layer II, where they combine with Hf ions to form acicular HfO_2, thus rendering it significantly more difficult for Nb to form oxides.

In light of the above results and discussions, the oxidation mechanism of the $TZHNF_{0.5}$ RHEA heated at 1000 °C is schematically depicted in Fig. 16. During the early process of oxidation, a $(TiZrHfNb)O_2$ composite oxide forms on the alloy surface, with the simple oxides TiO_2 and ZrO_2 rapidly formed because of the higher stability of the Ti and Zr element oxides, which share similar crystal structures and cation radii, leading to the formation of the composite oxide, Ti_2ZrO_6. However, Fe elements possess the highest diffusion coefficient, and rapidly diffuse through the Laves phase to the surface to react with oxygen, forming the protruding oxides of Fe_2O_3, which results in a rapid oxidation-weight gain and the generation of an outer oxide film.

With the increased heating duration and the development of a complete surface-oxide film, the oxidation-weight gain tends to plateau. During this period, Fe ions rapidly diffuse outward, leading to the generation of a Fe-depleted layer between the outer oxide film and the inner diffusion layer. Simultaneously, Nb has the slowest diffusion rate within the surface layer. At this point, the O ions have been consumed in the initial stage, and then react with Hf ions within the oxide layer to form acicular HfO_2 oxides, which precipitate between the oxide film and the inner metal, forming the inner oxide layer. Under long-term high-temperature environments, the internal microstructure of the alloy gradually refines, and concurrently, intermetallic compounds precipitate at the phase boundaries, giving rise to the formation of the matrix-transition layer and the original matrix layer.

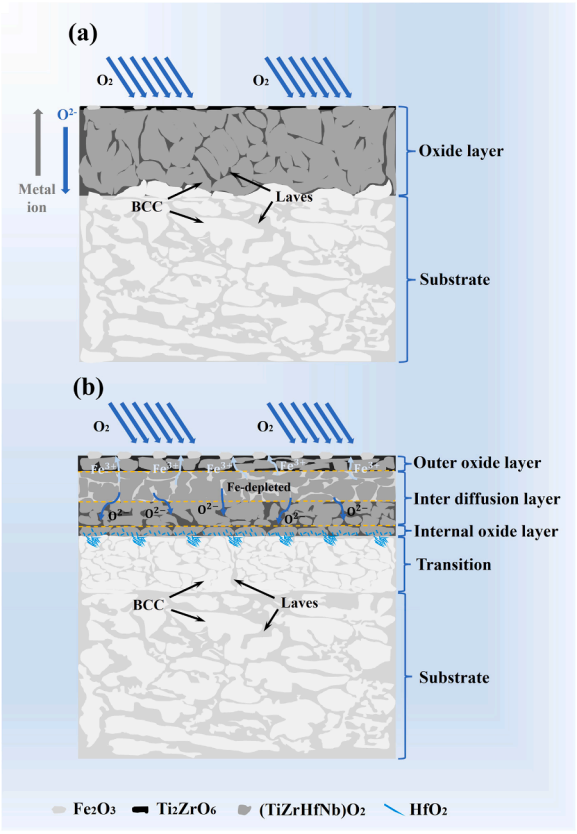

Fig. 16. Oxidation mechanisms of the $TZHNF_{0.5}$ RHEA heated at 1000 °C: (a) 1000 °C-starting, (b) 1000 °C-6 h.

5. Conclusion

The present work studies the oxidation behavior of the $TZHNF_{0.5}$ RHEA under different temperatures, as well as the impact of thermal oxidation on the hardness, sliding behavior, electrochemical characteristics, and surface bioactivity of the alloy. By analyzing the evolution of the oxidation layer's morphology and structure, the oxidation mechanisms were explored. The primary conclusions can be summarized as follows:

1. The $TZHNF_{0.5}$ RHEA exhibits "abnormal" oxidation behavior at 1000 °C, with an oxidation rate smaller than that at 800 °C and 1200 °C. At 1000 °C, the oxidation rate of the RHEA rapidly increases within the first 15 min, but notably decreases with increasing heating duration, resulting in the formation of a complete and dense surface oxide film.
2. Under different oxidation-temperature conditions, the $TZHNF_{0.5}$ RHEA exhibits the highest micro-Vickers hardness of 1146.64 Hv after oxidation at 1000 °C. It also demonstrates the lowest dry and wet friction wear rates, which are 3.23×10^{-9} $mm^3 \cdot mm^{-1} \cdot N^{-1}$ and 1.54×10^{-9} $mm^3 \cdot mm^{-1} \cdot N^{-1}$, respectively, representing a decrease of about two orders of magnitude, compared to the as-cast HEA, and indicating excellent wear resistance.
3. Under different oxidation-temperature conditions, the $TZHNF_{0.5}$ RHEA presents excellent corrosion resistance after oxidation at 1000 °C, with the highest corrosion potential, the lowest corrosion current density, the lowest passivation-current density, and good biocompatibility.
4. In the early oxidation stage of the $TZHNF_{0.5}$ RHEA, a Ti_2ZrO_6 composite oxide with a PBR value of 1.71 is formed, making the surface-oxide film more protective. Based on the principles of oxidation thermodynamics and kinetics, the dense oxide film inhibits the inward diffusion of oxygen ions and outward diffusion of metal cations in the oxide layer, thereby improving the oxidation resistance of the alloy.

Statement of originality

I would like to declare on behalf of my co-authors that the work described was original research that has not been published previously, and not under consideration for publication elsewhere, in whole or in part.

CRediT authorship contribution statement

Nengbin Hua: Writing – review & editing, Writing – original draft, Supervision, Resources, Project administration, Funding acquisition, Conceptualization. **Jun Shen:** Writing – review & editing, Conceptualization. **Qianting Wang:** Writing – review & editing. **Bozhuan Lin:** Writing – review & editing, Methodology, Investigation, Data curation. **Yang Xu:** Writing – original draft, Methodology, Investigation, Data curation. **Peter K. Liaw:** Writing – review & editing. **Xiongwei Liang:** Resources, Investigation. **Da Zeng:** Writing – review & editing, Resources. **Xinxiong Xiao:** Resources, Investigation. **Lei Zhang:** Writing – review & editing. **Hanxin Lin:** Methodology, Investigation, Formal analysis. **Pinqiang Dai:** Writing – review & editing, Investigation. **Wenfei Lu:** Writing – review & editing, Investigation.

Declaration of Competing Interest

The authors declare that they have no known competing financial interests or personal relationships that could have appeared to influence the work reported in this paper.

Data availability

Data will be made available on request.

Acknowledgement

The present work was supported by the Scientific Research Project of the Fujian Provincial Department of Science and Technology (2023H4031, 2022L3062 and 2021H0023), and the Scientific Research Project of the Fujian Provincial Department of Industry and Information Technology (2023G014), and the Scientific Research Project of Ningde Science and Technology Bureau (ND2023J006). P.K. Liaw also acknowledges the support from the National Science Foundation under grants DMR-1611180, 1809640 and 2226508.

Appendix A. Supporting information

Supplementary data associated with this article can be found in the online version at doi:10.1016/j.triboint.2024.110172.

References

[1] Sidhu SS, Singh H, Gepreel MAH. A review on alloy design, biological response, and strengthening of β-titanium alloys as biomaterials. Mater Sci Eng C 2021;121:111661. https://doi.org/10.1016/j.msec.2020.111661.
[2] Zhuang YF, Ren L, Zhang SY, Wei X, Yang K, Dai KR. Antibacterial effect of a copper-containing titanium alloy against implant-associated infection induced by methicillin-resistant Staphylococcus aureus. Acta Biomater 2021;119:472–84. https://doi.org/10.1016/j.actbio.2020.10.026.
[3] Guan SW, Qi M, Wang C, Wang SY, Wang WQ. Enhanced cytocompatibility of Ti6Al4V alloy through selective removal of Al and V from the hierarchical micro-arc oxidation coating. Appl Surf Sci 2021;541:148547. https://doi.org/10.1016/j.apsusc.2020.148547.
[4] Pobloth AM, Checa S, Razi H, Petersen A, Weaver JC, Schmidt-Bleek K, et al. Mechanobiologically optimized 3D titanium-mesh scaffolds enhance bone regeneration in critical segmental defects in sheep. Sci Transl Med 2018;10(423). https://doi.org/10.1126/scitranslmed.aam8828.

[5] Chen QZ, Thouas GA. Metallic implant biomaterials. Mater Sci Eng R 2015;87:1–57. https://doi.org/10.1016/j.mser.2014.10.001.

[6] Ehtemam-Haghighi S, Attar H, Dargusch MS, Kent D. Microstructure, phase composition and mechanical properties of new, low cost Ti-Mn-Nb alloys for biomedical applications. J Alloy Compd 2019;787:570–7. https://doi.org/10.1016/j.jallcom.2019.02.116.

[7] Zhang LC, Chen LY, Zhou SF, Luo Z. Powder bed fusion manufacturing of beta-type titanium alloys for biomedical implant applications: a review. J Alloy Compd 2023;936:168099. https://doi.org/10.1016/j.jallcom.2022.168099.

[8] Svanidze E, Besara T, Ozaydin MF, Tiwary CS, Wang JK, Radhakrishnan S, et al. High hardness in the biocompatible intermetallic compound β-Ti_3Au. Sci Adv 2016;2(7). https://doi.org/10.1126/sciadv.1600319.

[9] Hussain SA, Panchal M, Allamraju KV, Rajak U, Verma TN, Brindhadevi K. Optimization of wear behavior of heat-treated Ti-6Al-7Nb biomedical alloy by response surface methodology. Environ Res 2023;231:116193. https://doi.org/10.1016/j.envres.2023.116193.

[10] Geetha M, Singh AK, Asokamani R, Gogia AK. Ti based biomaterials, the ultimate choice for orthopaedic implants: a review. Prog Mater Sci 2009;54:397–425. https://doi.org/10.1016/j.pmatsci.2008.06.004.

[11] Liu X, Chu P, Ding C. Surface modification of titanium, titanium alloys, and related materials for biomedical applications. Mater Sci Eng R 2004;47:49–121. https://doi.org/10.1016/j.mser.2004.11.001.

[12] Weng WJ, Biesiekierski A, Lin JX, Ozan S, Li YC, Wen CE. Development of beta-type Ti-Nb-Zr-Mo alloys for orthopedic applications. Appl Mater Today 2021;22:100968. https://doi.org/10.1016/j.apmt.2021.100968.

[13] Cui SS, Liu S, Nie JJ, Chen DF, Wu XB, Qin GW, et al. Design and preparation of a biomedical titanium alloy with low elastic modulus and high antibacterial property based on Ti-Mo-Ag system. J Alloy Compd 2022;908:164639. https://doi.org/10.1016/j.jallcom.2022.164639.

[14] Liu DN, Xie HC, Ma ZC, Zhang W, Zhao HW, Ren LQ. Simultaneous enhancement of anti-friction and wear resistance performances via porous substrate and FeCoNiTiAl high entropy alloy coating of artificial joint materials. J Mater Res Technol 2022;19:2907–15. https://doi.org/10.1016/j.jmrt.2022.06.051.

[15] Ansari N, Lee DH, Huang EW, Jain J, Lee SY. Anisotropic microstructure, nanomechanical and corrosion behavior of direct energy deposited Ti-13Nb-13Zr biomedical alloy. J Mater Res Technol 2023;26:2682–94. https://doi.org/10.1016/j.jmrt.2023.08.015.

[16] Bahl S, Suwas S, Chatterjee K. Comprehensive review on alloy design, processing, and performance of β Titanium alloys as biomedical materials. Int Mater Rev 2021;66:114–39. https://doi.org/10.1080/09506608.2020.1735829.

[17] Quadros FD, Kuroda PAB, Sousa KDJ, Donato TAG, Grandini CR. Preparation, structural and microstructural characterization of Ti-25Ta-10Zr alloy for biomedical applications. J Mater Res Technol 2019;8:4108–14. https://doi.org/10.1016/j.jmrt.2019.07.020.

[18] Li PY, Ma XD, Tong T, Wang YS. Microstructural and mechanical properties of β-type Ti-Mo-Nb biomedical alloys with low elastic modulus. J Alloy Compd 2020;815:152412. https://doi.org/10.1016/j.jallcom.2019.152412.

[19] Hua NB, Wang WJ, Wang QT, Ye YX, Lin SH, Zhang L, et al. Mechanical, corrosion, and wear properties of biomedical Ti-Zr-Nb-Ta-Mo high entropy alloys. J Alloy Compd 2021;861:157997. https://doi.org/10.1016/j.jallcom.2020.157997.

[20] Hu SW, Li TJ, Li QL, Liu DX. Microstructure evolution, deformation mechanism, and mechanical properties of biomedical TiZrNb medium entropy alloy processed using equal channel angular pressing. Intermetallics 2022;151:107725. https://doi.org/10.1016/j.intermet.2022.107725.

[21] Shi YR, Wang W, Zhou Q, Xia QS, Hua DP, Huang ZY, et al. A molecular dynamics study on the defect formation and mechanical behavior of molybdenum disulfide under rrradiation. ACS Appl Mater Interfaces 2024;16:29453–65. https://doi.org/10.1021/acsami.4c05553.

[22] Correa DRN, Grandini CR, Rocha LA, Proença JP, Sottovia L, Cruz NC, et al. Effect of temperature on thermal oxidation behavior of biomedical Ti-Zr-Mo alloys. J Alloy Compd 2022;905:164202. https://doi.org/10.1016/j.jallcom.2022.164202.

[23] Zhou Q, Luo DW, Hua DP, Y WT, Li S, Zou QG, et al. Design and characterization of metallic glass/graphene multilayer with excellent nanowear properties. Friction 2022;10:1913–26. https://doi.org/10.1007/s40544-021-0581-6.

[24] Zhou Q, Xia QS, Li QK, Luo DW, Huang ZB, Wang CY, et al. Microstructure, mechanical and tribological properties of NbMoWTaAg refractory high entropy films with nano-layered self-organization. Tribol Int 2024;198:109888. https://doi.org/10.1016/j.triboint.2024.109888.

[25] Trivedi P, Gupta P, Srivastava S, Jayaganthan R, Chandra R, Roy P. Characterization and in vitro biocompatibility study of Ti-Si-N nanocomposite coatings developed by using physical vapor deposition. Appl Surf Sci 2014;293:143–50. https://doi.org/10.1016/j.apsusc.2013.12.119.

[26] Vazirgiantzikis I, George SL, Pichon L. Surface characterisation and silver release from Ti-6Al-4V and anodic TiO_2 after surface modification by ion implantation. Surf Coat Technol 2022;433:128115. https://doi.org/10.1016/j.surfcoat.2022.128115.

[27] Raghuram H, Katsich C, Pichelbauer K, Koschatzky K, Gachot C, Cihak-Bayr U. Design of wear and corrosion resistant FeNi-graphite composites by laser cladding. Surf Coat Technol 2019;377:124897. https://doi.org/10.1016/j.surfcoat.2019.124897.

[28] Latief FH, Sherif ESM, Wismogroho AS, Widayatno WB, Abdo HS. The cyclic oxidation and hardness characteristics of thermally exposed titanium prepared by inductive sintering-assisted powder metallurgy. Crystals 2020;10:104. https://doi.org/10.3390/cryst10020104.

[29] Zhong XY, Deng TS, Xiao WL, Zhong M, Lai YH, Ojo OA. Effect of minor Sc modification on the high-temperature oxidation behavior of near-α Ti alloy. Corros Sci 2023;217:111122. https://doi.org/10.1016/j.corsci.2023.111122.

[30] Wang S, Liao ZH, Liu YH, Liu WQ. Influence of thermal oxidation temperature on the microstructural and tribological behavior of Ti6Al4V alloy. Surf Coat Technol 2014;240:470–7. https://doi.org/10.1016/j.surfcoat.2014.01.004.

[31] Aniolek K, Kupka M. Mechanical, tribological and adhesive properties of oxide layers obtained on the surface of the Ti-6Al-7Nb alloy in the thermal oxidation process. Wear 2019;432-433:202929. https://doi.org/10.1016/j.wear.2019.202929.

[32] López MF, Jiménez JA, Gutiérrez A. Corrosion study of surface-modified vanadium-free titanium alloys. Electrochim Acta 2003;48:1395–401. https://doi.org/10.1016/S0013-4686(03)00006-9.

[33] Kumar S, Narayanan TSNS, Raman SGS, Seshadri SK. Thermal oxidation of CP Ti: an electrochemical and structural characterization. Mater Charact 2010;61:589–97. https://doi.org/10.1016/j.matchar.2010.03.002.

[34] Wang XQ, Zhang YS, Han WZ. Design of high strength and wear-resistance β-Ti alloy via oxygen-charging. Acta Mater 2022;227:117686. https://doi.org/10.1016/j.actamat.2022.117686.

[35] Güleryüz H, Çimenoğlu H. Effect of thermal oxidation on corrosion and corrosion–wear behaviour of a Ti-6Al-4V alloy. Biomaterials 2004;25:3325–33. https://doi.org/10.1016/j.biomaterials.2003.10.009.

[36] Wang S, Liao ZH, Liu YH, Liu WQ. Influence of thermal oxidation duration on the microstructure and fretting wear behavior of Ti6Al4V alloy. Mater Chem Phys 2015;159:139–51. https://doi.org/10.1016/j.matchemphys.2015.03.063.

[37] Aniolek K, Barylski A, Kupka M. Modelling the structure and mechanical properties of oxide layers obtained on biomedical Ti-6Al-7Nb alloy in the thermal oxidation process. Vacuum 2018;154:309–14. https://doi.org/10.1016/j.vacuum.2018.05.028.

[38] George EP, Raabe D, Ritchie RO. High-entropy alloys. Nat Rev Mater 2019;4:515–34. https://doi.org/10.1038/s41578-019-0121-4.

[39] Yeh JW, Chen SK, Lin SJ, Gan JY, Chin TS, Shun TT, et al. Nanostructured high-entropy alloys with multiple principal elements: novel alloy design concepts and outcomes. Adv Eng Mater 2004;6:299–303. https://doi.org/10.1002/adem.200300567.

[40] Tsai MH, Yeh JW. High-entropy alloys: a critical review. Mater Res Lett 2014;2:107–23. https://doi.org/10.1080/21663831.2014.912690.

[41] Cantor B, Chang ITH, Knight P, Vincent AJB. Microstructural development in equiatomic multicomponent alloys. Mater Sci Eng A 2004;375-377:213–8. https://doi.org/10.1016/j.msea.2003.10.257.

[42] Zhao GB, Shao XX, Zhang QX, Wu YL, Wang YN, Chen X, et al. Porous bio-high entropy alloy scaffolds fabricated by direct ink writing. J Mater Sci Technol 2023;157:21–9. https://doi.org/10.1016/j.jmst.2023.02.015.

[43] Huo WY, Fang F, Zhou H, Xie ZH, Shang JK, Jiang JQ. Remarkable strength of CoCrFeNi high-entropy alloy wires at cryogenic and elevated temperatures. Scr Mater 2017;141:125–8. https://doi.org/10.1016/j.scriptamat.2017.08.006.

[44] Tang Z, Yuan T, Tsai CW, Yeh JW, Lundin CD, Liaw PK. Fatigue behavior of a wrought $Al_{0.5}$CoCrCuFeNi two-phase high-entropy alloy. Acta Mater 2015;99:247–58. https://doi.org/10.1016/j.actamat.2015.07.004.

[45] Ye YF, Wang Q, Lu J, Liu CT, Yang Y. High-entropy alloy: challenges and prospects. Mater Today 2016;19:349–62. https://doi.org/10.1016/j.mattod.2015.11.026.

[46] Cantor B. Multicomponent high-entropy alloys. Prog Mater Sci 2021;120:100754. https://doi.org/10.1016/j.pmatsci.2020.100754.

[47] Gludovatz B, Hohenwarter A, Catoor D, Chang EH, George EP, Ritchie RO. A fracture-resistant high-entropy alloy for cryogenic applications. Science 2014;345:1153–8. https://doi.org/10.1126/science.1254581.

[48] Pan QS, Zhang LX, Feng R, Lu QH, An K, Chuang AC, et al. Gradient cell–structured high-entropy alloy with exceptional strength and ductility. Science 2021;374:984–9. https://doi.org/10.1126/science.abj8114.

[49] Shi PJ, Li RG, Li Y, Wen YB, Zhong YB, Ren WL, et al. Hierarchical crack buffering triples ductility in eutectic herringbone high-entropy alloys. Science 2021;373:912–8. https://doi.org/10.1126/science.abf6986.

[50] Li TS, Swanson OJ, Frankel GS, Gerard AY, Lu P, Saal JE, et al. Localized corrosion behavior of a single-phase non-equimolar high entropy alloy. Electrochim Acta 2019;306:71–84. https://doi.org/10.1016/j.electacta.2019.03.104.

[51] Bhattacharyya JJ, Inman SB, Wischhusen MA, Qi J, Poon J, Scully JR, et al. Lightweight, low cost compositionally complex multiphase alloys with optimized strength, ductility and corrosion resistance: Discovery, design and mechanistic understandings. Mater Des 2023;228:111831. https://doi.org/10.1016/j.matdes.2023.111831.

[52] Shi YZ, Yang B, Liaw PK. Corrosion-resistant high-entropy alloys: a review. Metals 2017;7:43. https://doi.org/10.3390/met7020043.

[53] Zhou EZ, Qiao DX, Yang Y, Xu DK, Lu YP, Wang JJ, et al. A novel Cu-bearing high-entropy alloy with significant antibacterial behavior against corrosive marine biofilms. J Mater Sci Technol 2020;46:201–10. https://doi.org/10.1016/j.jmst.2020.01.039.

[54] Shi YZ, Yang B, Xie X, Brechtl J, Dahmen KA, Liaw PK. Corrosion of Al_xCoCrFeNi high-entropy alloys: Al-content and potential scan-rate dependent pitting behavior. Corros Sci 2017;119:33–45. https://doi.org/10.1016/j.corsci.2017.02.019.

[55] Senkov ON, Senkova SV, Woodward C. Effect of aluminum on the microstructure and properties of two refractory high-entropy alloys. Acta Mater 2014;68:214–28. https://doi.org/10.1016/j.actamat.2014.01.029.

[56] Li XL, Li HZ, Li Q, Jin C, Hua K, Wang HF. The determining role of Al addition on tribology properties and oxidation behavior at elevated temperatures of TiZrHfNb refractory high-entropy alloy. Mater Charact 2022;189:111921. https://doi.org/10.1016/j.matchar.2022.111921.

[57] Jayaraj J, Thirathipviwat P, Han J, Gebert A. Microstructure, mechanical and thermal oxidation behavior of AlNbTiZr high entropy alloy. Intermetallics 2018; 100:9–19. https://doi.org/10.1016/j.intermet.2018.05.015.
[58] Xu XC, Li Z, Lai WJ, Wang BB, Xu QH, Zhang ZG, et al. Improved wear and corrosion resistance of biomedical TiZrNbTaMo medium-entropy alloy by thermal oxidation treatment. Tribol Int 2023;189:108897. https://doi.org/10.1016/j.triboint.2023.108897.
[59] Wang WJ, Yang KH, Wang QT, Dai PQ, Fang H, Wu FJ, et al. Novel Ti-Zr-Hf-Nb-Fe refractory high-entropy alloys for potential biomedical applications. J Alloy Compd 2022;906:164383. https://doi.org/10.1016/j.jallcom.2022.164383.
[60] Liu YY, Chen Z, Chen YZ, Shi JC, Wang ZY, Wang S, et al. Effect of Al content on high temperature oxidation resistance of Al_xCoCrCuFeNi high entropy alloys (x=0, 0.5, 1, 1.5, 2). Vacuum 2019;169:108837. https://doi.org/10.1016/j.vacuum.2019.108837.
[61] Birks N, Meier GH, Pettit FS. Introduction to the High Temperature Oxidation of Metals. second ed..,. Cambridge: Cambridge University Press; 2006. https://doi.org/10.1017/CBO9781139163903.
[62] Senkov ON, Senkova SV, Dimiduk DM, Woodward C, Miracle DB. Oxidation behavior of a refractory $NbCrMo_{0.5}Ta_{0.5}TiZr$ alloy. J Mater Sci 2012;47:6522–34. https://doi.org/10.1007/s10853-012-6582-0.
[63] Butler TM, Chaput KJ, Dietrich JR, Senkov ON. High temperature oxidation behaviors of equimolar NbTiZrV and NbTiZrCr refractory complex concentrated alloys (RCCAs). J Alloy Compd 2017;729:1004–19. https://doi.org/10.1016/j.jallcom.2017.09.164.
[64] Zhao P, Li J, Zhang Y, Li X, Xia MM, Yuan BG. Wear and high-temperature oxidation resistances of $AlNbTaZr_x$ high-entropy alloys coatings fabricated on Ti6Al4V by laser cladding. J Alloy Compd 2021;862:158405. https://doi.org/10.1016/j.jallcom.2020.158405.
[65] Sheikh S, Gan L, Ikeda A, Murakami H, Guo S. Alloying effect on the oxidation behavior of a ductile $Al_{0.5}Cr_{0.25}Nb_{0.5}Ta_{0.5}Ti_{1.5}$ refractory high-entropy alloy. Mater Today Adv 2020;7:100104. https://doi.org/10.1016/j.mtadv.2020.100104.
[66] Sheikh S, Bijaksana MK, Motallebzadeh A, Shafeie S, Lozinko A, Gan L, et al. Accelerated oxidation in ductile refractory high-entropy alloys. Intermetallics 2018;97:58–66. https://doi.org/10.1016/j.intermet.2018.04.001.
[67] Hua NB, Qian ZY, Lin BZ, Liao ZL, Wang QT, Dai PQ, et al. Formation of a protective oxide layer with enhanced wear and corrosion resistance by heating the $TiZrHfNbFe_{0.5}$ refractory multi-principal element alloy at 1,000 °C. Scr Mater 2023;225:115165. https://doi.org/10.1016/j.scriptamat.2022.115165.
[68] Ouyang D, Chen ZJ, Yu HB, Chan KC, Liu L. Oxidation behavior of the $Ti_{38}V_{15}Nb_{23}Hf_{24}$ refractory high-entropy alloy at elevated temperatures. Corros Sci 2022;198:110153. https://doi.org/10.1016/j.corsci.2022.110153.
[69] Wu MY, Diao GJ, Yuan J, Fraser D, Li J, Chung R, et al. Corrosion and corrosive wear of AlCrFeCoNi and Co-free AlCrFeNi-Ti_x (x=0-1.5) high-entropy alloys in 3.5 wt% NaCl and H_2SO_4 (pH=3) solutions. Wear 2023;523:204765. https://doi.org/10.1016/j.wear.2023.204765.
[70] Metikoš-Huković M, Kwokal A, Piljac J. The influence of niobium and vanadium on passivity of titanium-based implants in physiological solution. Biomaterials 2003; 24:3765–75. https://doi.org/10.1016/S0142-9612(03)00252-7.
[71] Hua NB, Chen WZ, Zhang L, Li GH, Liao ZL, Lin Y. Mechanical properties and biotribological behaviors of novel beta-Zr-type Zr-Al-Fe-Nb alloys for biomedical applications. Mater Sci Eng C 2017;76:1154–65. https://doi.org/10.1016/j.msec.2017.02.146.
[72] Balakrishnan S, Padmanabhan VP, Kulandaivelu R, Nellaiappan T, Sagadevan S, Paiman S, et al. Influence of iron doping towards the physicochemical and biological characteristics of hydroxyapatite. Ceram Int 2021;47:5061–70. https://doi.org/10.1016/j.ceramint.2020.10.084.
[73] Shi HS, Yang SY, Zeng SH, Liu X, Zhang J, Zhang J, et al. Enhanced angiogenesis of biodegradable iron-doped octacalcium phosphate/poly(lactic-co-glycolic acid) scaffold for potential cancerous bone regeneration. Appl Mater Today 2019;15: 100–14. https://doi.org/10.1016/j.apmt.2019.01.002.
[74] Gorr B, Schellert S, Müller F, Christ HJ, Kauffmann A, Heilmaier M. Current status of research on the oxidation behavior of refractory high entropy alloys. Adv Eng Mater 2021;23:2001047. https://doi.org/10.1002/adem.202001047.
[75] Müller F, Gorr B, Christ HJ, Müller J, Butz B, Chen H, et al. On the oxidation mechanism of refractory high entropy alloys. Corros Sci 2019;159:108161. https://doi.org/10.1016/j.corsci.2019.108161.
[76] Kumaresan L, Prabhu A, Palanichamy M, Arumugam E, Murugesan V. Synthesis and characterization of Zr^{4+}, La^{3+} and Ce^{3+} doped mesoporous TiO_2: evaluation of their photocatalytic activity. J Hazard Mater 2011;186:1183–92. https://doi.org/10.1016/j.jhazmat.2010.11.124.
[77] Lin Y, Guo Y, Dong Q, Huang R, Tan J. Effects of vanadium content on the high temperature oxidation behavior of NbTiZrAlV refractory complex concentrated alloys. J Alloy Compd 2022;905:164180. https://doi.org/10.1016/j.jallcom.2022.164180.
[78] Pilling N, Bedworth RJ. The oxidation of metals at high temperatures. J Inst Met 1923;29:529.
[79] Kubaschewski O, Hopkins BE. Oxidation of metals and alloys. 2nd ed. New York: Academic Press; 1962.
[80] Li YT, Zhang P, Zhang JY, Chen Z, Shen BL. Oxidation behavior of $AlCoCrFeNiSi_x$ high-entropy alloys at 1100 °C. Corros Sci 2021;190:109633. https://doi.org/10.1016/j.corsci.2021.109633.
[81] Yang XM, An ZB, Zhai YD, Wang X, Chen YH, Mao SC, et al. Effect of Al content on the thermal oxidation behaviour of AlHfMoNbTi high-entropy alloys analysed by in situ environmental TEM. Corros Sci 2021;191:109711. https://doi.org/10.1016/j.corsci.2021.109711.
[82] Yang DN, Liu Y, Han TY, Zhou F, Qu N, Liao MQ, et al. High thermal stability and oxidation behavior of FeCrNiAl-based medium-entropy alloys prepared by powder metallurgy. J Alloy Compd 2022;918:165562. https://doi.org/10.1016/j.jallcom.2022.165562.
[83] Sharma R, Roy A, De PS. Equimolar AlCuFeMn: a novel oxidation resistant alloy. Intermetallics 2021;135:107215. https://doi.org/10.1016/j.intermet.2021.107215.
[84] Dong ZQ, Sun AK, Yang S, Yu XD, Yuan H, Wang ZH, et al. Machine learning-assisted discovery of Cr, Al-containing high-entropy alloys for high oxidation resistance. Corros Sci 2023;220:111222. https://doi.org/10.1016/j.corsci.2023.111222.
[85] Cui Y, Shen JQ, Manladan SM, Geng KP, Hu SS. Wear resistance of $FeCoCrNiMnAl_x$ high-entropy alloy coatings at high temperature. Appl Surf Sci 2020;512:145736. https://doi.org/10.1016/j.apsusc.2020.145736.
[86] Li MS, Qian YH, Li X. Volume ratio of an oxide to the metal. Corros Sci Prot Technol 1999;11:284–9.
[87] Li CL, Song P, Khan A, Feng J, Chen KL, Zang JJ, et al. Influence of water vapour on the HfO_2 distribution within the oxide layer on CoNiCrAlHf alloys. J Alloy Compd 2018;739:690–9. https://doi.org/10.1016/j.jallcom.2017.12.334.
[88] Behnamian Y, Mostafaei A, Kohandehghan A, Amirkhiz BS, Serate D, Sun YF, et al. A comparative study of oxide scales grown on stainless steel and nickel-based superalloys in ultra-high temperature supercritical water at 800 °C. Corros Sci 2016;106:188–207. https://doi.org/10.1016/j.corsci.2016.02.004.
[89] Zou DN, Zhou YQ, Zhang X, Zhang W, Han Y. High temperature oxidation behavior of a high Al-containing ferritic heat-resistant stainless steel. Mater Charact 2018; 136:435–43. https://doi.org/10.1016/j.matchar.2017.11.038.
[90] Zhang WL, Li SM, Fu LB, Li W, Sun J, Wang TG, et al. Preparation and cyclic oxidation resistance of Hf-doped NiAl coating. Corros Sci 2022;195:110014. https://doi.org/10.1016/j.corsci.2021.110014.
[91] Hu GX, Cai X, Rong YH. Fundamentals of Materials Science. 3d ed. Shanghai: Shanghai Jiao Tong University Press; 2010.
[92] Wagner C. Theoretical analysis of the diffusion processes determining the oxidation rate of alloys. J Electrochem Soc 1952;99:369–80. https://doi.org/10.1149/1.2779605.
[93] Li TF. High temperature oxidation and hot corrosion of metals. 1st ed. Beijing: Chemical Industry Press; 2003.